Variational quantitative phase-field modeling of nonisothermal sintering process

Timileyin David Oyedeji [1,*] Yangyiwei Yang [1,†] Herbert Egger [2] and Bai-Xiang Xu [1,‡]

[1]*Mechanics of Functional Materials Division, Institute of Materials Science, Technische Universität Darmstadt, 64287 Darmstadt, Germany*

[2]*Johann Radon Institute for Computational and Applied Mathematics and Institute for Computational Mathematics, Johannes-Kepler University Linz, 4040 Linz, Austria*

(Received 23 May 2023; accepted 21 June 2023; published 4 August 2023)

Phase-field modeling has become a powerful tool in describing the complex pore-structure evolution and the intricate multiphysics in nonisothermal sintering processes. However, the quantitative validity of conventional variational phase-field models involving diffusive processes is a challenge. Artificial interface effects, like the trapping effects, may originate at the interface when the kinetic properties of two opposing phases are different. On the other hand, models with prescribed antitrapping terms do not necessarily guarantee the thermodynamics variational nature of the model. This issue has been solved for liquid-solid interfaces via the development of the variational quantitative solidification phase-field model. However, there is no related work addressing the interfaces in nonisothermal sintering, where the free surfaces between the solid phase and surrounding pore regions exhibit strong asymmetry of mass and thermal properties. Also, additional challenges arise due to the conserved order parameter describing the free surfaces. In this work, we present a variational and quantitative phase-field model for nonisothermal sintering processes. The model is derived via an extended nondiagonal phase-field model. The model evolution equations have naturally cross-coupling terms between the conserved kinetics (i.e., mass and thermal transfer) and the nonconserved one (grain growth). These terms are shown via asymptotic analysis to be instrumental in ensuring the elimination of interface artifacts, while also examined to not modify the thermodynamic equilibrium condition (characterized by a dihedral angle). Moreover, we demonstrate that the trapping effects and the existence of surface diffusion in conservation laws are direction-dependent. An anisotropic interpolation scheme of the kinetic mobilities that differentiates between the normal and tangential directions along the interface is discussed. Numerically, we demonstrate the importance of the cross-couplings and the anisotropic interpolation by presenting thermal-microstructural evolutions.

DOI: 10.1103/PhysRevE.108.025301

I. INTRODUCTION

Sintering is a typical densification technique in thermal processing of bulk materials from packed powders [1–3]. At present, many new techniques based on sintering have been proposed and broadly applied in the industry, where the thermal bonding effect is introduced by treatments other than direct heating, such as laser scan, electrical current, and electromagnetic field [3–6]. These techniques are collectively termed "unconventional" sintering [7,8]. Due to the distinct heating mechanisms among unconventional sintering techniques, the effects of nonisothermal factors on the properties of products, such as the heating/cooling rate and temperature inhomogeneity, have gained increasing attention alongside those of conventional techniques such as the chemical composition as well as the size of powders, atmosphere, and pressure.

Therefore, it is essential to identify and understand the physical effects and interactions of these factors in the context of bridging the process parameters, microstructure, and properties of the materials to further tailor the performance for applications of interest. Two major types of interfaces are essential for the sintering process, namely the free surface between pore and substance, and the grain boundary between adjacent crystal grains. There are analytical models for describing the evolution of pores/grains, the two-particle coalescence model [9,10], the dodeca-/tetrakaidecahedron grain model [11], and various models treating the pores/grains through assumed geometries such as spheres or cylinders [12,13]. Nevertheless, complex grain/pore geometry and entangled multiple physics during sintering exceeds the capacity of these models.

For such purposes, phase-field modeling and simulation are promising. In the conventional variational phase-field theory, order parameters (OPs) are applied to represent the spatiotemporal distribution of microstructure, i.e., pores and grain orientations in the case of sintering. The thermodynamic potential of the microstructure can then be formulated by an energy functional with respect to the OPs, including the interface contribution through the corresponding gradient terms of OPs. From nonequilibrium thermodynamics, the evolution equations of the OPs can be derived on the basis of the variational theory. It circumvents the necessity of interface tracking. There are variational phase-field sintering models considering an isothermal scenario. For instance, Kazaryan *et al.* [14] and Wang [15] proposed a line of a phase-field model, which was used later for studying

*timileyin.oyedeji@tu-darmstadt.de
†yangyiwei.yang@mfm.tu-darmstadt.de
‡xu@mfm.tu-darmstadt.de

two-particle necking and coalescence [16–22] and densification of a porous microstructure [17,23], and in simulating the overall microstructure evolution of the particle aggregation [24] or particle stack [15,25]. Rigid-body motions were also incorporated within the model [15,20,21,25]. Furthermore, a phase-field sintering model adopting the grand potential concept was also developed [26,27]. To simulate the sintering process under a highly heterogeneous thermal environment, the phase-field sintering model coupled with transient heat and/or chemical diffusion simulations are needed. The phase-field approach allows such a consideration through additive inclusion of the energy contributions by the related physical fields, such as temperature or chemical concentration. In our previous work [28], a variational nonisothermal phase-field sintering model was proposed, which was applied for simulations of the selective laser sintering on single-layer and multilayer [29] powder beds, and for sintering under a prescribed high-temperature gradient [8].

On the other hand, one theoretical issue of the conventional variational phase-field models involving the thermal/chemical diffusive process is the quantitative validity. Artificial interface effects may originate from violation of conservation laws and discontinuity of the chemical/thermal potentials at the interface (trapping effects) [30,31]. These interface effects scale with the interface width. Theoretically, via asymptotic analysis, phase-field models should be reduced to their associated free-boundary problems in order to ensure their quantitative validity. Based on thin-interface limit analysis, Karma and Rappel [32,33] first published a quantitative phase-field model for the solidification of pure materials with equal diffusivities in the solid and liquid phases. Moreover, by introducing an antitrapping term in the diffusion flux equation in order to eliminate the trapping effect, Karma [34] presented a quantitative model for the case of isothermal solidification of alloys with negligible diffusivity in the solid phase. Furthermore, for the case with arbitrarily different diffusivities in opposing phases, corresponding antitrapping terms have also been proposed for isothermal [35] and nonisothermal consideration [36]. Thereby, a new parameter relating the interface velocity and diffusion flux was further introduced to ensure full elimination of all interface artifacts.

It should be noted that modifying a variationally derived evolution equation by prescribed antitrapping terms does not necessarily guarantee the variational nature of the model, which is, however, important for thermodynamics soundness. Therefore, there have been efforts to develop variational formulations of quantitative phase-field models. Using phenomenological linear relations, variational formulation of quantitative phase-field models has been developed by considering kinetic cross-coupling between the conserved diffusion fields and the nonconserved OPs (nondiagonal model) [37–40]. Time evolution equations of the models then exhibit cross-coupling kinetic terms that are formulated in a similar fashion due to Onsager's symmetry. Furthermore, the parameters of these coupling terms are explicitly formulated in terms of the model parameters by considering the relations between the models and their sharp-interface counterparts. The cross-coupling term in the diffusion equations, which can be likened to the antitrapping term alongside the coupling term in the phase-field evolution equations, has been noted to enable full elimination of artificial interface effects [40,41]. The nondiagonal model has been employed to investigate quantitative phase-field simulations of dendritic growth [42] and to examine quantitative simulations of eutectic and eutectoid transformations [43] in which the necessity of the cross-coupling terms was substantiated in both instances.

By separately considering the thermodynamic quantities of two opposing phases and then treating the interface as a mixture of the phases (two-phase variational approach), Ohno *et al.* [44,45] presented quantitative variational phase-field models for binary alloy solidification with two-sided diffusion. In the two-phase formulation, the diffusion field mixture laws are ensured at the interface as constraints implemented by the Lagrange multiplier approach, and the flux fields of each single-phase field are formulated variationally. The emergence of Lagrange multipliers in the thermodynamic potential formulation gives rise to cross-coupling terms in the model time evolution equations that serve to eliminate the artificial interface effects. Additionally, the necessity of an anisotropic interpolation of the diffusivity (different interpolations for the normal and the tangential directions across the diffuse interface) is demonstrated in eliminating the anomalous interface effects. Though the two-phase variational approach is promising for the study of quantitative validity, the variational nature of the model is only implicitly implemented through variationally formulated single-phase fluxes. The variational behavior of the final model after inserting the Lagrange multiplier still needs to be examined. Moreover, due to the assumptions of a negligible temperature jump or a chemical potential jump across the diffuse interface, the models in Refs. [44,45] are applicable mostly for slow solidification processes.

Based on a literature review, there is currently no variational quantitative phase-field model for nonisothermal sintering. In comparison to the nonisothermal solidification models with nonconserved OPs, an additional challenge can be expected due to the conserved OPs involved here. In this work, we derive a variational formulation of a quantitative phase-field model for nonisothermal sintering processes in which the free surfaces between the solid phase and the surrounding atmosphere/pore regions have strong asymmetry of both mass and thermal properties. The model is derived via an extension of the nondiagonal phase-field model. Different from the conventional variational nonisothermal sintering phase-field models, the derived model contains cross-coupling terms in the diffusion and phase-field evolution equations, which are essential to ensure the quantitative validity of the model. Furthermore, we demonstrate that the existence of the trapping effects and the presence of surface diffusion in conservation laws are direction-dependent. This highlights the need for an anisotropic interpolation of the diffusivity tensor.

The paper is structured as follows. The formulations of the quantitative model (denoted as the "quantitative model" hereafter) are derived in Sec. II, where the entropy functional and time evolution equations are explicitly given. A sharp-interface description across solid free surfaces is briefly explained in Sec. III. Afterwards, a linkage between model parameters and sharp-interface equations using a reduction procedure is demonstrated in Sec. IV. Section V shows the

verification and importance of the quantitative model followed by a comparison with the nonisothermal sintering model proposed in our former work (denoted as the "existing model" hereafter). Conclusions are presented in Sec. VI.

II. MODEL FORMULATION

Underlying physical processes involved in nonisothermal sintering can be classified as, but not limited to, (a) the mass/heat transport, including diffusion through sorts of paths (volume, surface, and grain boundaries) and mass flows (viscous or fluid flow); (b) the structural relaxation, including the rigid-body motions of powders and interface (mostly the grain boundaries) migration. All underlying interactive processes collectively lead to two significant phenomena: one is the densification (eliminating the pores), in which the total surface energy should be reduced; the other is the grain coarsening, in which the total grain-boundary energy should decrease [1,2,46]. In the following, we then present a framework for deriving the nonisothermal variational quantitative phase-field sintering model, with its quantitative validity engendered by asymptotic analysis.

A. Entropy and free-energy functionals

In this model, a conserved OP ρ denoting the solid density fraction is used to indicate the solid region ($\rho = 1$) and the atmosphere/pores region ($\rho = 0$) while a series of nonconserved OPs $\{\eta_i\}$ are used to represent the different grain orientations of the solid grains. Considering a nonisothermal scenario, the entropy functional S for a subdomain Ω within the sintering system is defined as

$$S(e,\rho,\{\eta_i\}) = \int_\Omega \left[s(e,\rho,\{\eta_i\}) - \frac{\kappa_\rho}{2}|\nabla\rho|^2 - \frac{\kappa_\eta}{2}\sum_i |\nabla\eta_i|^2 \right] d\Omega,$$

with

$$s = \frac{1+h(\rho)}{2}s_{\rm ss}(e_{\rm ss}) + \frac{1-h(\rho)}{2}s_{\rm at}(e_{\rm at}) + s_{\rm cf}(\rho,\{\eta_i\}), \quad (1)$$

where s is the local entropy density, e is the internal energy density, while κ_ρ and κ_η are the gradient energy coefficients associated with ρ and $\{\eta_i\}$, respectively. $s_{\rm ss}$ is the solid phase bulk entropy density and is dependent on the internal energy density of the solid $e_{\rm ss}$. The bulk entropy density of the atmosphere $s_{\rm at}$ is dependent on the internal energy density of the atmosphere $e_{\rm at}$. $h(\rho) = 2\rho - 1$ is an interpolation function. The configurational entropy $s_{\rm cf}$ is related to the spatial distribution of entropy density proportional to ρ and $\{\eta_i\}$. It is formulated in the form of a Landau-type polynomial similar to the one given by Ref. [15] as

$$s_{\rm cf}(\rho,\{\eta_i\}) = \underline{C}_{\rm cf}[\rho^2(1-\rho)^2] + \underline{D}_{\rm cf}\left[\rho^2 + 6(1-\rho)\times\sum_i \eta_i^2 - 4(2-\rho)\sum_i \eta_i^3 + 3\left(\sum_i \eta_i^2\right)^2\right], \quad (2)$$

where $\underline{C}_{\rm cf}$ and $\underline{D}_{\rm cf}$ are constants. The multiwell potential in Eq. (2) can be seen to exhibit minimally at various regions such as atmosphere ($\rho = 0$, $\{\eta_1 = 0,\ldots,\eta_n = 0\}$) and solid grains at different orientations ($\rho = 1$, $\{\eta_1 = 1,\ldots,\eta_n = 0\}$), …, ($\rho = 1$, $\{\eta_1 = 0,\ldots,\eta_n = 1\}$). One advantage of this potential form is that its constant parameters can be directly linked to material properties [17].

Assume e can be expressed as

$$e = \frac{1+h(\rho)}{2}e_{\rm ss} + \frac{1-h(\rho)}{2}e_{\rm at} + e_{\rm pt}(\rho,\{\eta_i\}), \quad (3)$$

where $e_{\rm pt}$ accounts for the spatial distribution of the internal energy proportional to ρ and $\{\eta_i\}$ and is also formulated similar to $s_{\rm cf}$ as

$$e_{\rm pt}(\rho,\{\eta_i\}) = \underline{C}_{\rm pt}[\rho^2(1-\rho)^2] + \underline{D}_{\rm pt}\left[\rho^2 + 6(1-\rho)\times\sum_i \eta_i^2 - 4(2-\rho)\sum_i \eta_i^3 + 3\left(\sum_i \eta_i^2\right)^2\right], \quad (4)$$

where $\underline{C}_{\rm pt}$ and $\underline{D}_{\rm pt}$ are constants.

Following the Legendre transformation, we can obtain the free-energy functional F as

$$F(T,\rho,\{\eta_i\}) = \int_\Omega \left[f(T,\rho,\{\eta_i\}) + \frac{T\kappa_\rho}{2}|\nabla\rho|^2 + \frac{T\kappa_\eta}{2}\sum_i |\nabla\eta_i|^2 \right] d\Omega, \quad (5)$$

with

$$f(T,\rho,\{\eta_i\}) = \frac{1+h(\rho)}{2}f_{\rm ss}(T) + \frac{1-h(\rho)}{2}f_{\rm at}(T) + e_{\rm pt} - Ts_{\rm cf}, \quad (6)$$

where $f_{\rm ss}$ and $f_{\rm at}$ are the free-energy densities of the solid phase and the atmosphere, respectively, and T is the temperature. Substituting Eqs. (2) and (4) into Eq. (6), we obtain

$$f(T,\rho,\{\eta_i\}) = \frac{1+h(\rho)}{2}f_{\rm ss}(T) + \frac{1-h(\rho)}{2}f_{\rm at}(T) + \underline{C}[\rho^2(1-\rho)^2] + \underline{D}\left[\rho^2 + 6(1-\rho)\times\sum_i \eta_i^2 - 4(2-\rho)\sum_i \eta_i^3 + 3\left(\sum_i \eta_i^2\right)^2\right], \quad (7)$$

with

$$\underline{C} = \underline{C}_{\rm pt} - T\underline{C}_{\rm cf},$$
$$\underline{D} = \underline{D}_{\rm pt} - T\underline{D}_{\rm cf}.$$

B. Kinetic equations

Considering that ρ and e are conserved OPs, they satisfy mass and energy conservation laws, respectively:

$$\dot{\rho} = -\nabla \cdot \mathbf{J}_\rho, \tag{8}$$

$$\dot{e} = -\nabla \cdot \mathbf{J}_e, \tag{9}$$

where $\mathbf{J}_\rho$ is the mass diffusion flux and $\mathbf{J}_e$ is the energy flux.

Following our previous work [8], the non-negative entropy production σ in the subdomain can be formulated as

$$\sigma = \int_\Omega \left[\mathbf{J}_\rho \cdot \nabla \frac{\delta S}{\delta \rho} + \mathbf{J}_e \cdot \nabla \frac{\delta S}{\delta e} + \sum_i \dot{\eta}_i \frac{\delta S}{\delta \eta_i} \right] d\Omega, \tag{10}$$

with

$$\frac{\delta S}{\delta \rho} = -\frac{1}{T}\frac{\delta F}{\delta \rho}, \ \frac{\delta S}{\delta \eta_i} = -\frac{1}{T}\frac{\delta F}{\delta \eta_i}, \ \frac{\delta S}{\delta e} = \frac{1}{T},$$

where $\nabla(\delta S/\delta\rho)$ is the driving force associated with $\mathbf{J}_\rho$, $\nabla(\delta S/\delta e)$ is the driving force associated with $\mathbf{J}_e$, and $\delta S/\delta\eta_i$ is the driving force associated with $\dot{\eta}_i$.

In view of the phenomenological linear laws of nonequilibrium thermodynamics and also ensuring non-negative production of the entropy, we can define the relationships between the fluxes, the nonconserved OPs time evolution equations, and their driving forces as

$$\begin{bmatrix} \mathbf{J}_\rho \\ \mathbf{J}_e \\ \dot{\eta}_1 \\ \vdots \\ \dot{\eta}_n \end{bmatrix} = \begin{bmatrix} \mathbf{L}_{\rho\rho} & \mathbf{L}_{\rho e} & \mathbf{L}_{\rho\eta_1} & \cdots & \mathbf{L}_{\rho\eta_n} \\ \mathbf{L}_{e\rho} & \mathbf{L}_{ee} & \mathbf{L}_{e\eta_1} & \cdots & \mathbf{L}_{e\eta_n} \\ \mathbf{L}_{\eta_1\rho} & \mathbf{L}_{\eta_1 e} & \mathbf{L}_{\eta_1\eta_1} & \cdots & \mathbf{L}_{\eta_1\eta_n} \\ \vdots & \vdots & \vdots & \ddots & \vdots \\ \mathbf{L}_{\eta_n\rho} & \mathbf{L}_{\eta_n e} & \mathbf{L}_{\eta_n\eta_1} & \cdots & \mathbf{L}_{\eta_n\eta_n} \end{bmatrix} \begin{bmatrix} -\nabla\left(\frac{\mu}{T}\right) \\ \nabla\left(\frac{1}{T}\right) \\ \frac{\delta S}{\delta \eta_1} \\ \vdots \\ \frac{\delta S}{\delta \eta_n} \end{bmatrix}, \tag{11}$$

where $\mu = \delta F/\delta\rho$ is defined as the chemical potential and n represents the total number of grain orientations. $\mathbf{L}_{\rho\rho}$, $\mathbf{L}_{\rho e}$, $\mathbf{L}_{e\rho}$, and $\mathbf{L}_{ee}$ are positively defined rank 2 tensors, and for $i = 1, 2, \ldots, n$, $\mathbf{L}_{\rho\eta_i}$, $\mathbf{L}_{e\eta_i}$, $\mathbf{L}_{\eta_i\rho}$, and $\mathbf{L}_{\eta_i,e}$ are positively defined rank 1 tensors while $\mathbf{L}_{\eta_i\eta_i}$ is a positively defined rank 0 tensor.

Diagonal terms $\mathbf{L}_{\rho\rho}$ and $\mathbf{L}_{ee}$ are the diffusional mobilities of mass and energy diffusion, respectively. The mobility term associated with the grain orientations, $\mathbf{L}_{\eta_i\eta_i}$, is simply a scalar function and is thereafter taken as L_η where we assume an isotropic condition taking it to be the same regardless of i. The nondiagonal terms in the Onsager matrix in Eq. (11) represent cross-couplings between the various OPs. Based on the Onsager reciprocal relations, we have $\mathbf{L}_{\rho e} = \mathbf{L}_{e\rho}$, $\mathbf{L}_{\rho\eta_i} = \mathbf{L}_{\eta_i\rho}$, and $\mathbf{L}_{e\eta_i} = \mathbf{L}_{\eta_i e}$. Note that the cross-coupling between the different grain orientations is not considered, resulting in similar $\dot{\eta}_i$ formulation for all i. Hence we consider only one $\dot{\eta}_i$ whose formulation is representative for all i. The quantities $\mathbf{L}_{\rho e}$ and $\mathbf{L}_{e\rho}$ are associated with the mass flux due to temperature gradient (thermophoresis effect) and with the energy flux due to chemical potential gradient (Dufour effect), respectively. Examination of these effects has been done in our previous work [8] and is not the main priority of this work. Therefore, the terms associated with $\mathbf{L}_{\rho e}$ and $\mathbf{L}_{e\rho}$ in the fluxes formulations are dropped. The time evolution equations can then be written as

$$\dot{\rho} = \nabla \cdot \left[\mathbf{L}_{\rho\rho} \cdot \nabla\left(\frac{\mu}{T}\right) \right] + \nabla \cdot \left[\frac{1}{T} \sum_i \mathbf{L}_{\rho\eta_i} \frac{\delta F}{\delta \eta_i} \right], \tag{12a}$$

$$\dot{e} = \nabla \cdot \left[\mathbf{L}_{\mathrm{ee}} \cdot \frac{\nabla T}{T^2} \right] + \nabla \cdot \left[\frac{1}{T} \sum_i \mathbf{L}_{e\eta_i} \frac{\delta F}{\delta \eta_i} \right], \tag{12b}$$

$$\dot{\eta}_i = -\mathbf{L}_{\eta_i\rho} \cdot \nabla\left(\frac{\mu}{T}\right) - \mathbf{L}_{\eta_i,e} \cdot \frac{\nabla T}{T^2} - L_\eta \frac{1}{T}\frac{\delta F}{\delta \eta_i}. \tag{12c}$$

Formulations expressed in Eqs. (11) and (12) present the fluxes and time evolution equations of the associated OPs in terms of the driving forces. However, for consistency with previous nondiagonal models [38,40] as well as ease of relating our model to the sharp-interface counterpart, as will be discussed later, we reformulate the phenomenological linear relations employing the linear relations of the driving forces in terms of the fluxes and time evolution equations such that

$$-\nabla\left(\frac{\mu}{T}\right) = \mathbf{L}_{\rho\rho}^{-1} \cdot \mathbf{J}_\rho + \mathbf{L}_{\rho\eta_i}^{-1} \sum_i \dot{\eta}_i, \tag{13a}$$

$$-\frac{\nabla T}{T^2} = \mathbf{L}_{\mathrm{ee}}^{-1} \cdot \mathbf{J}_e + \mathbf{L}_{e\eta_i}^{-1} \sum_i \dot{\eta}_i, \tag{13b}$$

$$-\frac{1}{T}\frac{\delta F}{\delta \eta_i} = \mathbf{L}_{\eta_i\rho}^{-1} \cdot \mathbf{J}_\rho + \mathbf{L}_{\eta_i,e}^{-1} \cdot \mathbf{J}_e + L_\eta^{-1} \dot{\eta}_i. \tag{13c}$$

Since the variation of mass density and internal energy is found across free surfaces of the solid grains, the cross-coupling terms $\mathbf{L}_{\rho\eta_i}^{-1} = \mathbf{L}_{\eta_i\rho}^{-1}$ and $\mathbf{L}_{e\eta_i}^{-1} = \mathbf{L}_{\eta_i e}^{-1}$ should be defined such that they are only evaluated at the free surfaces. Also, the nonequilibrium effects associated with these cross terms scale with the diffuse interface width l. Accordingly, following Refs. [37,38,40], we propose the following formulations:

$$\mathbf{L}_{\rho\eta_i}^{-1} = \mathbf{L}_{\eta_i\rho}^{-1} = M_1(\rho) l \nabla \rho, \tag{14a}$$

$$\mathbf{L}_{e\eta_i}^{-1} = \mathbf{L}_{\eta_i e}^{-1} = M_2(\rho) l \nabla \rho, \tag{14b}$$

where M_1 and M_2 are scalar functions used to parametrize the associated cross-coupling terms. $l\nabla\rho$ is a vector normal to the free surfaces and has a magnitude of 1 at the center of the free surfaces assuming the parameter α used to adjust the definition of l in Ref. [47] equals 2 [28]. Substituting Eq. (13) into (10) and taking into account the aforementioned, we obtain the entropy production in the subdomain as

$$\sigma = \int_\Omega \left[\mathbf{L}_{\rho\rho}^{-1} \cdot \mathbf{J}_\rho \cdot \mathbf{J}_\rho + \mathbf{L}_{\mathrm{ee}}^{-1} \cdot \mathbf{J}_e \cdot \mathbf{J}_e + L_\eta^{-1} \left(\sum_i \dot{\eta}_i \right)^2 + 2 l \nabla \rho \sum_i \dot{\eta}_i \cdot (M_1 \mathbf{J}_\rho + M_2 \mathbf{J}_e) \right] d\Omega. \tag{15}$$

Furthermore, time evolution equations can be obtained as

$$\dot{\rho} = \nabla \cdot \left[\mathbf{L}_{\rho\rho} \cdot \left(\nabla\left(\frac{\mu}{T}\right) + M_1 l \nabla \rho \sum_i \dot{\eta}_i \right) \right], \tag{16a}$$

$$c_{\mathrm{r}} \dot{T} + \frac{\partial e}{\partial \rho}\dot{\rho} + \sum_i \frac{\partial e}{\partial \eta_i}\dot{\eta}_i = \nabla \cdot \left[\mathbf{L}_{\mathrm{ee}} \cdot \left(\frac{\nabla T}{T^2} + M_2 l \nabla \rho \sum_i \dot{\eta}_i \right) \right], \tag{16b}$$

$$\hat{L}_\eta^{-1}\dot{\eta}_i = \kappa_\eta \nabla^2 \eta_i - \frac{1}{T}\frac{\partial f}{\partial \eta_i} + l\nabla\rho \cdot \left[M_1 \mathbf{L}_{\rho\rho} \cdot \nabla\left(\frac{\mu}{T}\right) + M_2 \mathbf{L}_{ee} \cdot \frac{\nabla T}{T^2}\right], \quad (16c)$$

with

$$\hat{L}_\eta^{-1} = L_\eta^{-1} - [M_1^2 l^2 \nabla\rho \cdot \mathbf{L}_{\rho\rho} + M_2^2 l^2 \nabla\rho \cdot \mathbf{L}_{ee}] \cdot \nabla\rho. \quad (17)$$

Hereby $c_r = \frac{1+h(\rho)}{2}c_{ss} + \frac{1-h(\rho)}{2}c_{at}$ is the relative specific heat, where $c_{ss} = \partial e_{ss}/\partial T$ and $c_{at} = \partial e_{at}/\partial T$ are the volumetric specific heat of solid and atmosphere, respectively.

Comparing the heat-transfer equation [Eq. (16b)] to that of conventional quantitative phase-field model [36], the second term on the right-hand side (RHS) can be likened to the thermal antitrapping current related to the elimination of thermal trapping (associated with temperature jump) at the free surfaces. Similarly, the second term on the RHS of Eq. (16a) represents some form of antitrapping current valued only at the free surfaces. Similar to solutal antitrapping current [34,48] associated with solute trapping due to a jump of chemical potential, this term is termed as the mass antitrapping current in this work. The last two terms on the RHS of the grain orientation time evolution equations [Eq. (16c)] represent cross-coupling terms associated with mass and energy diffusion across the free surfaces, respectively. These terms alongside the antitrapping terms are absent in time evolution equations of conventional nonisothermal phase-field sintering models but are very vital in the elimination of artificial interface effects such as the trapping effects at the free surfaces of the solid phase.

Moreover, considering no variation of solid density and thermal properties across the grain boundaries, Eq. (16c) has no cross-coupling terms and simply takes a form of the Allen-Cahn equation at the grain boundaries. Consequently, we limit our subsequent analysis and derivations to the free surfaces where the cross-coupling terms are significant.

III. SHARP-INTERFACE DESCRIPTION ACROSS FREE SURFACES

Considering a simple nonisothermal system consisting of a sharp free surface between a solid grain and the atmosphere, the following set of sharp-interface equations can be described in the bulk regions:

$$\frac{\partial \rho}{\partial t} = \nabla \cdot (M_{rg}\nabla\mu), \quad (18)$$

$$c_{rg}\frac{\partial T}{\partial t} = \nabla \cdot (k_{rg}\nabla T), \quad (19)$$

where for a bulk region rg ("ss" for solid and "at" for atmosphere), M_{rg}, c_{rg}, and k_{rg} represent the region's effective-mass mobility coefficient, volumetric specific heat, and effective thermal conductivity, respectively. ρ here adopts the physical meaning of normalized density of the solid. Equations (18) and (19) describe mass and heat transfer in the bulk regions. For the bulk atmosphere region in particular, M_{at} describes the effective mobility considering mass transfer mechanisms, notably evaporation and condensation. Hence, the driving force $\nabla\mu$ for mass transfer in the atmosphere takes into account vapor pressure differences due to local curvature [1,2]. Similarly, k_{at} describes effective thermal conductivity taking into account convection and radiation.

Furthermore, the energy conservation condition at the free surface can be described as

$$v e_{ss} + k_{ss}\nabla T|_{ss} \cdot \mathbf{n}_{sf} = v e_{at} + k_{at}\nabla T|_{at} \cdot \mathbf{n}_{sf} = J_T, \quad (20)$$

where v is the velocity of the migrating free surface, and $\nabla T|_{ss}$ and $\nabla T|_{at}$ are the spatial gradients of the temperature at the solid and atmosphere sides of the free surface, respectively. $\mathbf{n}_{sf}$ is the unit vector normal to the free surface. J_T is the normal heat flux flowing through the free surface. Similarly, explicit formulation of mass conservation at the free surface is given as

$$v(\rho_{ss} - \rho_{at}) = -M_{ss}\nabla\mu|_{ss} \cdot \mathbf{n}_{sf} + M_{at}\nabla\mu|_{at} \cdot \mathbf{n}_{sf} + M_{sf}\nabla_{sf}^2\mu, \quad (21)$$

where ρ_{ss} and ρ_{at} are the bulk densities in the solid and atmosphere, and $\nabla\mu|_{ss}$ and $\nabla\mu|_{at}$ are the spatial gradients of the chemical potential at the solid and atmosphere sides of the free surface, respectively. M_{sf} represents surface diffusion mobility. ∇_{sf}^2 is a surface Laplacian. The last term in Eq. (21) describes surface diffusion typical of a sharp-interface description of mass transfer in sintering [18]. Moreover, v can be defined as

$$v = v_s + v_b, \quad (22)$$

where v_s and v_b are the velocities contributed by surface diffusion and bulk/volume diffusion, respectively, and they can be expressed in terms of their corresponding mass fluxes,

$$v_s = -V_m\nabla_{\mathbf{sf}} \cdot \mathbf{J}_{sf}, \quad v_b = -V_m\mathbf{J}_b \cdot \mathbf{n}_{sf}, \quad (23)$$

where V_m is the molar volume and $\nabla_{\mathbf{sf}}$ is the surface gradient. $\mathbf{J}_{sf}$ is the mass flux along the free surface associated with the surface gradient of the free surface curvature k_{sf}; $\mathbf{J}_{sf} \propto \nabla_{\mathbf{sf}}k_{sf}$. $\mathbf{J}_b$ is mass flux from the solid bulk to the free surface associated with the gradient of the chemical potential in the solid bulk grains μ_{ss}; $\mathbf{J}_b \propto \nabla\mu_{ss}$ [18,49].

In addition, the chemical potential and temperature at the free surface obey the following relations:

$$\mu|_{ss} = \mu|_{at}, \quad (24a)$$

$$T|_{ss} - T|_{at} = J_T R_s, \quad (24b)$$

where $\mu|_{ss}$ and $\mu|_{at}$ represent chemical potentials at the solid and atmosphere sides of the free surface, respectively. $T|_{ss}$ and $T|_{at}$ represent the temperatures at the solid and atmosphere sides of the free surface, respectively. R_s represents Kapitza-type thermal resistance. In this work, we assume negligible R_s, thereby Eqs. (24a) and (24b) indicate the imposed zero chemical potential and temperature jumps at the free surface.

Moreover, we infer that the jump in chemical potential $\delta\mu$ across the free surface is conjugated to v and also that the temperature jump δT across the free surface is conjugated to J_T. The kinetic boundary conditions can then be expressed in the framework of phenomenological linear relations as [50,51]

$$\delta\mu = \mathcal{A}v + \mathcal{B}J_T, \quad (25)$$

$$\delta T = \mathcal{B}v + \mathcal{C}J_T, \quad (26)$$

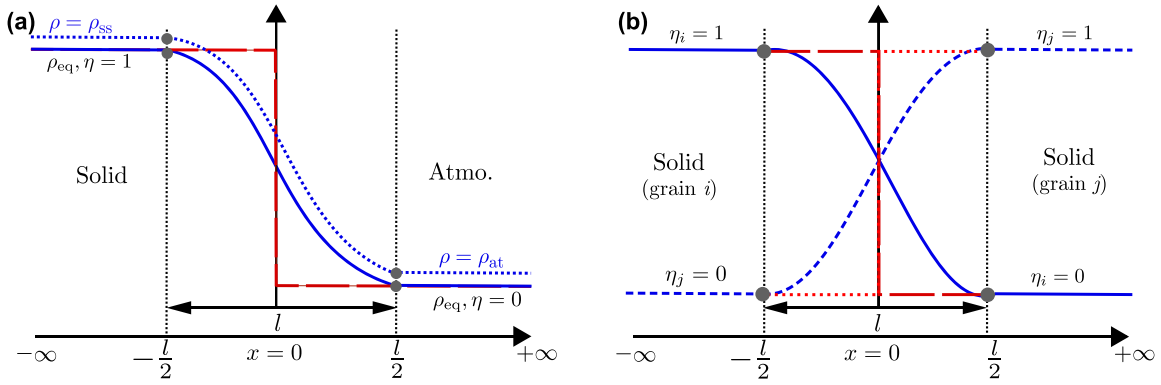

FIG. 1. (a) Asymptotic schematic across a free surface; the blue solid line represents the phase-field profile at equilibrium, and the red large-dashed line represents the sharp-interface profile; the blue dotted line shows the profile of ρ with slightly deviated values. (b) Asymptotic schematic across a grain boundary; blue solid and dashed lines represent phase-field profiles, and red large-dashed and dotted lines represent sharp-interface profiles.

where $\mathcal{A}$, $\mathcal{B}$, and $\mathcal{C}$ are kinetic coefficients of the positive-definite Onsager matrix. Entropy production at the free surface σ_s can be formulated as

$$\sigma_s = v\delta\mu + J_T\delta T. \tag{27}$$

Substituting Eqs. (25) and (26) into (27), we obtain

$$\sigma_s = \mathcal{A}v^2 + \mathcal{C}J_T^2 + 2\mathcal{B}vJ_T. \tag{28}$$

IV. THIN INTERFACE LIMIT: LINKING MODEL WITH SHARP-INTERFACE DESCRIPTION

In this section, still considering a system consisting of a free surface between a solid grain and the atmosphere, we establish the relationships between $\mathcal{A}$, $\mathcal{B}$, and $\mathcal{C}$ and the phase-field parameters following the reduction procedure presented in Ref. [38]. Considering a 1D system with the free surface centered at $x = 0$ [shown in Fig. 1(a)], we have ρ and η vary from a semifinite solid region $(-\infty)$ to a semifinite atmosphere region $(+\infty)$. For simplicity, the notation $(\cdot)'$ is adopted to represent the derivative with respect to the spatial coordinate x. It is worth noting that we consider the profile of ρ between two bulk values that are slightly deviated from the ideal ones, i.e., ρ_{ss} in the substance and ρ_{at} in the pore/atmosphere. The origin and the thermodynamic outcome of these deviated bulk values of ρ are explicitly examined and discussed in the Appendix.

According to the phase-field method, the entropy production [Eq. (15)] for the system considered can be formulated as

$$\begin{aligned}\sigma = &\int_{-\infty}^{-l/2}\left[\frac{J_\rho^2(x)}{L_{\rho\rho}^{ss}} + \frac{J_e^2(x)}{L_{ee}^{ss}}\right]dx + \int_{l/2}^{\infty}\left[\frac{J_\rho^2(x)}{L_{\rho\rho}^{at}} + \frac{J_e^2(x)}{L_{ee}^{at}}\right]dx \\ &+ \int_{-l/2}^{l/2}\left[\frac{J_\rho^2(x)}{L_{\rho\rho}} + \frac{J_e^2(x)}{L_{ee}} + L_{\eta,sf}^{-1}\dot{\eta}^2 \right.\\ &\left. + 2l\rho'(x)\dot{\eta}[M_1J_\rho(x) + M_2J_e(x)]\right]dx,\end{aligned} \tag{29}$$

where $L_{\rho\rho}^{ss} = L_{\rho\rho}(\rho = \rho_{ss})$ and $L_{\rho\rho}^{at} = L_{\rho\rho}(\rho = \rho_{at})$ are the effective-mass mobilities in the corresponding regions. Also, $L_{ee}^{ss} = L_{ee}(\rho = \rho_{ss})$ and $L_{ee}^{at} = L_{ee}(\rho = \rho_{at})$ are the effective energy mobilities in the corresponding regions. $L_{\eta,sf}$ is the mobility of η at the free surface. It can be noted that in the bulk regions $(|x| > l/2)$, only the fluxes $J_\rho(x)$ and $J_e(x)$ contribute to entropy production as $\dot{\eta}$ and $\rho'(x)$ both go to zero. The entropy production of the system considered can be formulated within the sharp-interface description as

$$\int_{-\infty}^{0}\left[\frac{J_\rho^2(x)}{L_{\rho\rho}^{ss}} + \frac{J_e^2(x)}{L_{ee}^{ss}}\right]dx + \int_{0}^{\infty}\left[\frac{J_\rho^2(x)}{L_{\rho\rho}^{at}} + \frac{J_e^2(x)}{L_{ee}^{at}}\right]dx + \sigma_s. \tag{30}$$

Comparing Eqs. (29) and (30), we obtain entropy production at the free surface within the phase-field model as

$$\begin{aligned}\sigma_s = &\int_{-l/2}^{l/2}\left[\frac{J_\rho^2(x)}{L_{\rho\rho}} + \frac{J_e^2(x)}{L_{ee}} + L_{\eta,sf}^{-1}\dot{\eta}^2 + 2l\rho'(x)\dot{\eta}(M_1J_\rho(x)\right.\\ &\left. + M_2J_e(x))\right]dx - \int_{-l/2}^{0}\left[\frac{J_{ss(\rho)}^2}{L_{\rho\rho}^{ss}} + \frac{J_{ss(e)}^2}{L_{ee}^{ss}}\right]dx\\ &- \int_{0}^{l/2}\left[\frac{J_{at(\rho)}^2}{L_{\rho\rho}^{at}} + \frac{J_{at(e)}^2}{L_{ee}^{at}}\right]dx,\end{aligned} \tag{31}$$

where for a region rg ("ss" for solid and "at" for atmosphere), $J_{rg(\rho)}$ and $J_{rg(e)}$ represent the region's bulk mass and energy fluxes, respectively.

For the purpose of making direct relations between Eq. (31) and its sharp-interface counterpart, Eq. (28), we express $J_\rho(x)$, $J_e(x)$, and $\dot{\eta}$ in terms of v and J_T. First, we perform an analysis considering only fluxes that are flowing through the free surface along the x direction (i.e., normal to the free surface), thereby we tentatively drop the contribution of the surface diffusion flux J_{sf} to v since it is tangential to the free surface. Second, we employ a quasisteady approximation that assumes large gradients of ρ, e, and η across the free surface such that we define their time derivatives as

$$\dot{\rho} \approx -v\rho'(x),\ \dot{e} \approx -ve'(x),\ \dot{\eta} \approx -v\eta'(x). \tag{32}$$

We integrate both sides of the conservation laws, $\dot{e} = -J_e'(x)$ and $\dot{\rho} = -J_\rho'(x)$, after substituting Eq. (32),

$$\int_{J_{ss(\rho)}}^{J_{at(\rho)}} dJ_\rho = v\int_{\rho_{eq}^{ss}}^{\rho_{eq}^{at}} d\rho, \quad \int_{J_{ss(e)}}^{J_{at(e)}} dJ_e = v\int_{e_{eq}^{ss}}^{e_{eq}^{at}} de \tag{33}$$

with the boundary values as

$$\begin{aligned} J_{\mathrm{ss}(\rho)} &\approx v\rho_{\mathrm{eq}}^{\mathrm{ss}}, & J_{\mathrm{at}(\rho)} &\approx v\rho_{\mathrm{eq}}^{\mathrm{at}}, \\ J_{\mathrm{ss}(e)} &\approx ve_{\mathrm{eq}}^{\mathrm{ss}} - J_T, & J_{\mathrm{at}(e)} &\approx ve_{\mathrm{eq}}^{\mathrm{at}} - J_T, \end{aligned} \tag{34}$$

where $\rho_{\mathrm{rg}}^{\mathrm{eq}}$ and $e_{\mathrm{rg}}^{\mathrm{at}}$ (rg = ss, at) are the equilibrium conserved OP and internal energies, respectively. The integrals in Eq. (33) yield

$$J_e(x) \approx ve(x) - J_T, \quad J_\rho(x) \approx v\rho(x). \tag{35}$$

Furthermore, we adopt the sigmoid formulation for the profiles of $\rho(x)$ and $\eta(x)$ in this work as

$$\rho(x) = \frac{1}{2}\left[(\rho_{\mathrm{ss}} + \rho_{\mathrm{at}}) + (\rho_{\mathrm{ss}} - \rho_{\mathrm{at}})\tanh\frac{2x}{l}\right], \tag{36}$$

$$\eta(x) = \frac{1}{2}\left[1 + \tanh\left(\frac{2x}{l}\right)\right] \tag{37}$$

with the diffuse interface width l. Taking into account all the aforementioned, we obtain σ_s as

$$\begin{aligned} \sigma_s = &\int_{-l/2}^{l/2}\left[\frac{[v\rho(x)]^2}{L_{\rho\rho}} - \frac{(v\rho_{\mathrm{ss}})^2}{2L_{\rho\rho}^{\mathrm{ss}}} - \frac{(v\rho_{\mathrm{at}})^2}{2L_{\rho\rho}^{\mathrm{at}}}\right]dx \\ &+ \int_{-l/2}^{l/2}\left[\frac{[ve(x) - J_T]^2}{L_{\mathrm{ee}}} - \frac{(ve_{\mathrm{ss}} - J_T)^2}{2L_{\mathrm{ee}}^{\mathrm{ss}}}\right. \\ &\left. - \frac{(ve_{\mathrm{at}} - J_T)^2}{2L_{\mathrm{ee}}^{\mathrm{at}}}\right]dx - \int_{-l/2}^{l/2} 4l\rho'(x)\eta'(x)v \\ &\times [M_1[v\rho(x)] + M_2[ve(x) - J_T]]\,dx \\ &+ \int_{-l/2}^{l/2} L_{\eta,\mathrm{sf}}^{-1}v^2[\eta'(x)]^2\,dx. \end{aligned} \tag{38}$$

It should be noted that the integration range of Eq. (38) can also be taken from $-\infty$ and $+\infty$ without σ_s changing. In this regard, we extend the integration interval from $[-l/2, +l/2]$ to $[-\infty, +\infty]$ in the following discussion. Comparing Eqs. (28) and (38), we obtain

$$\begin{aligned} \mathcal{A} = &\int_{-\infty}^{\infty}\left[\frac{\rho^2(x)}{L_{\rho\rho}} - \frac{(\rho_{\mathrm{ss}})^2}{2L_{\rho\rho}^{\mathrm{ss}}} - \frac{(\rho_{\mathrm{at}})^2}{2L_{\rho\rho}^{\mathrm{at}}}\right]dx - 4 \\ &\times \int_{-\infty}^{\infty} M_1 l\rho'(x)\eta'(x)\rho(x)\,dx \\ &+ \int_{-\infty}^{\infty}\left[\frac{e^2(x)}{L_{\mathrm{ee}}} - \frac{(e_{\mathrm{ss}})^2}{2L_{\mathrm{ee}}^{\mathrm{ss}}} - \frac{(e_{\mathrm{at}})^2}{2L_{\mathrm{ee}}^{\mathrm{at}}}\right]dx - 4 \\ &\times \int_{-\infty}^{\infty} M_2 l\rho'(x)\eta'(x)e(x)\,dx \\ &+ \int_{-\infty}^{\infty} L_{\eta,\mathrm{sf}}^{-1}[\eta'(x)]^2\,dx, \end{aligned} \tag{39}$$

$$\begin{aligned} \mathcal{B} = &\int_{-\infty}^{\infty} 2M_2 l\rho'(x)\eta'(x)\,dx \\ &- \int_{-\infty}^{\infty}\left[\frac{e(x)}{L_{\mathrm{ee}}} - \frac{e_{\mathrm{ss}}}{2L_{\mathrm{ee}}^{\mathrm{ss}}} - \frac{e_{\mathrm{at}}}{2L_{\mathrm{ee}}^{\mathrm{at}}}\right]dx, \end{aligned} \tag{40}$$

$$\mathcal{C} = \int_{-\infty}^{\infty}\left[\frac{1}{L_{\mathrm{ee}}} - \frac{1}{2L_{\mathrm{ee}}^{\mathrm{ss}}} - \frac{1}{2L_{\mathrm{ee}}^{\mathrm{at}}}\right]dx. \tag{41}$$

The explicit formulations of $\mathcal{A}$, $\mathcal{B}$, and $\mathcal{C}$ imply that the phase-field parameters can be carefully tuned so as to obtain $\mathcal{A} = 0$, $\mathcal{B} = 0$, and $\mathcal{C} = 0$, which guarantees $\delta\mu = 0$ and $\delta T = 0$ across a migrating free surface. However, Almgren [30] has shown that conservation laws reproduced by phase-field models with asymmetric mobilities can be altered by two effects, namely interface stretching and surface diffusion, even though $\delta\mu = \delta T = 0$ is guaranteed. In the sintering system, interface stretching represents excess mass and internal energy along the arclength of the free surfaces of the solid phase [48], and these excesses can both be eliminated if $\int_{-\infty}^{\infty} dx[\rho - \rho_{\mathrm{ss}}/2 - \rho_{\mathrm{at}}/2] = 0$ and $\int_{-\infty}^{\infty} dx[e - e_{\mathrm{ss}}/2 - e_{\mathrm{at}}/2] = 0$, respectively [30,40]. Taking ρ as defined in Eq. (36) ensures that the interface excess of ρ is eliminated. Also, the interface excess of e is eliminated if $h(\rho)$ is taken as an odd function. Furthermore, surface diffusion terms in the mass and energy conservation laws at the free surfaces of the solid are parametrized, respectively, by the mobilities $L_{\rho\rho}^{\mathrm{sf}} = \int_{-\infty}^{\infty} dx[L_{\rho\rho}(\rho) - L_{\rho\rho}^{\mathrm{ss}}/2 - L_{\rho\rho}^{\mathrm{at}}/2]$ and $L_{\mathrm{ee}}^{\mathrm{sf}} = \int_{-\infty}^{\infty} dx[L_{\mathrm{ee}}(\rho) - L_{\mathrm{ee}}^{\mathrm{ss}}/2 - L_{\mathrm{ee}}^{\mathrm{at}}/2]$ [30,40].

To make $\delta T = 0$, we need to ensure that $\mathcal{B} = \mathcal{C} = 0$. Consequently, L_{ee} should be formulated such that it gives the bulk region energy mobilities at the corresponding regions, ensures $\mathcal{C} = 0$, and also guarantees that the model replicates the sharp-interface energy conservation law [Eq. (20)] where there is no surface diffusion effect (i.e., $L_{\mathrm{ee}}^{\mathrm{sf}} = 0$). To achieve this, Almgren [30] proposed a mobility interpolation function that is a combination of odd functions with parameters adjusted relative to the bulk mobilities. This method is contended by Ohno *et al.* [44] as the mobility interpolation function produces a nonmonotonic function and also contributes to a limited ratio of the possible bulk mobilities. Nevertheless, it is vital to note that while simultaneous elimination of δT and the surface diffusion effect put somewhat of a constraint on a scalar formulation of L_{ee}, the emergence of both effects is actually direction-dependent [52]. An L_{ee} formulation constraint due to δT [Eq. (41)] emerges under the consideration of flux components normal to the free surfaces as seen in the analysis done above, while the integral associated with the surface diffusion effect modification of energy conservation emanates due to consideration of flux components in the tangential direction to the free surfaces [52]. Therefore, ensuring $\mathcal{C} = 0$ and eliminating the surface diffusion term in the energy conservation equation, respectively, are pertinent only at the normal and tangential directions of the free surfaces. Considering all the aforementioned details and also taking into account the physical context of the energy mobility, we propose an anisotropic $\mathbf{L}_{\mathrm{ee}}$ for the full sintering description and relate it to the anisotropic thermal conductivity as

$$\begin{aligned} \mathbf{L}_{\mathrm{ee}} &= [k_\perp \mathbf{N}_{\mathrm{sf}} + k_\parallel \mathbf{T}_{\mathrm{sf}} + k_{\mathrm{gb}}\mathbf{T}_{\mathrm{gb}}]T^2 \\ &= L_{\mathrm{ee}}^{\perp}\mathbf{N}_{\mathrm{sf}} + L_{\mathrm{ee}}^{\parallel}\mathbf{T}_{\mathrm{sf}} + L_{\mathrm{ee}}^{\mathrm{gb}}\mathbf{T}_{\mathrm{gb}}, \end{aligned} \tag{42}$$

with

$$k_\perp = \left[\frac{1 + g(\rho)}{2k_{\mathrm{ss}}} + \frac{1 - g(\rho)}{2k_{\mathrm{at}}}\right]^{-1}, \tag{43}$$

$$k_\parallel = \frac{1 + g(\rho)}{2}k_{\mathrm{ss}} + \frac{1 - g(\rho)}{2}k_{\mathrm{at}}, \tag{44}$$

$$k_{\mathrm{gb}} = 16\sum_{i\neq j}\eta_i^2\eta_j^2 k_{\mathrm{gb}}, \tag{45}$$

and

$$\mathbf{N}_{\rm sf} = \mathbf{n}_{\rm sf} \otimes \mathbf{n}_{\rm sf},$$
$$\mathbf{T}_{\rm sf} = \mathbf{I} - \mathbf{n}_{\rm sf} \otimes \mathbf{n}_{\rm sf},$$
$$\mathbf{T}_{\rm gb} = \mathbf{I} - \mathbf{n}_{\rm gb} \otimes \mathbf{n}_{\rm gb}. \tag{46}$$

In Eq. (42), $L_{\rm ee}^{\perp}$ is the energy mobility in the normal direction to the free surfaces defined to ensure $\mathcal{C} = 0$, $L_{\rm ee}^{\parallel}$ is the energy mobility in the tangential direction to the free surfaces formulated to ensure $L_{\rm ee}^{\rm sf} = 0$ in the energy conservation law, and $L_{\rm ee}^{\rm gb}$ represents the energy mobility in the grain boundary. Similarly, $k_{\perp}$ and $k_{\parallel}$ represent the thermal conductivities at the normal and tangential directions to the free surfaces, respectively, while $k_{\rm gb}$ represent the thermal conductivity in the grain boundary. $k_{\rm ss}$ and $k_{\rm at}$ are, respectively, the effective thermal conductivities in the solid phase and the atmosphere region, and $k_{\rm gb}$ is the effective thermal conductivity in the grain boundary. Surface and grain boundary normal vectors are calculated from the gradient of corresponding OPs, e.g., $\mathbf{n}_{\rm sf} \equiv \nabla\rho/|\nabla\rho|$. $\mathbf{I}$ is the identity tensor and $\otimes$ represents the dyadic product. $g(\rho) = 2\rho - 1$ is an odd function that satisfies $g(\rho = \rho_{\rm ss}) = 1$ and $g(\rho = \rho_{\rm at}) = -1$.

Noting that $L_{\rm ee}^{\perp} = k_{\perp}T^2$ and therefore substituting Eq. (43) into (40), we obtain

$$\mathcal{B} = 2\chi M_2 - \frac{\beta l}{2T^2}\left(\frac{1}{2k_{\rm ss}} - \frac{1}{2k_{\rm at}}\right), \tag{47}$$

with

$$\chi = l\int_{-\infty}^{\infty} \rho'(x)\eta'(x)\,dx = 2(\rho_{\rm ss} - \rho_{\rm at})/3, \tag{48}$$
$$\beta = \frac{e_{\rm ht}}{l}\int_{-\infty}^{\infty} [h(\rho)g(\rho) - 1]\,dx = -e_{\rm ht}(\rho_{\rm ss} - \rho_{\rm at})^2, \tag{49}$$

where $e_{\rm ht} = e_{\rm ss} - e_{\rm at}$. The functions defined in Eqs. (37) and (36) are adopted to calculate integrals in Eqs. (48) and (49).

Therefore, to obtain $\mathcal{B} = 0$, we take

$$M_2 = \frac{\beta l}{4\chi T^2}\left(\frac{1}{2k_{\rm ss}} - \frac{1}{2k_{\rm at}}\right). \tag{50}$$

Following [8,17,53] whereby the different mass diffusion routes in the sintering process, i.e., bulk/volume diffusion, surface diffusion along the free surfaces, and grain boundary diffusion are taken into account, we propose an anisotropic $\mathbf{L}_{\rho\rho}$ and relate it to the anisotropic diffusivity as

$$\mathbf{L}_{\rho\rho} = [D_{\rm v}\mathbf{I} + D_{\rm sf}\mathbf{T}_{\rm sf} + D_{\rm gb}\mathbf{T}_{\rm gb}]/s_{\rm v}$$
$$= L_{\rho\rho}^{\rm v}\mathbf{I} + L_{\rho\rho}^{\rm sf}\mathbf{T}_{\rm sf} + L_{\rho\rho}^{\rm gb}\mathbf{T}_{\rm gb}, \tag{51}$$

with

$$D_{\rm v} = \left[\frac{1 + g(\rho)}{2D_{\rm ss}} + \frac{1 - g(\rho)}{2D_{\rm at}}\right]^{-1}, \tag{52}$$
$$D_{\rm sf} = 16\rho^2(1-\rho)^2 D_{\rm sf}, \tag{53}$$
$$D_{\rm gb} = 16\sum_{i\neq j}\eta_i^2\eta_j^2 D_{\rm gb}, \tag{54}$$

and the volumetric entropy as

$$s_{\rm v} = \frac{1}{T}\frac{\partial\mu}{\partial\rho}, \tag{55}$$

where the linear approximation is sometimes taken as $s_{\rm v} \approx \mathcal{R}/V_{\rm m}$ with the ideal gas constant $\mathcal{R}$ and molar volume $V_{\rm m}$ [8,17,54]. In Eq. (51), $L_{\rho\rho}^{\rm v}$ is the mass mobility in the normal direction to the free surfaces associated with the bulk/volume diffusion in solid phase and atmosphere region, and $L_{\rho\rho}^{\rm sf}$ is the mass mobility in the tangential direction to the free surfaces associated with mass transport via surface diffusion. Consideration of $L_{\rho\rho}^{\rm sf}$ ensures that the model replicates the sharp-interface mass conservation law Eq. (21) where surface diffusion is considered. $L_{\rho\rho}^{\rm gb}$ represent the mass mobility in the grain boundary. Similarly, $D_{\rm v}$ represents the volume diffusivity, which is interpolated by the effective diffusivities in the solid phase ($D_{\rm ss}$) and atmosphere region ($D_{\rm at}$). $D_{\rm sf}$ and $D_{\rm gb}$ are the effective diffusivities in the free surfaces and grain boundary, respectively.

We propose M_1 to have a similar form to that of M_2 in Eq. (50),

$$M_1 = -\frac{3ls_{\rm v}}{16}\left(\frac{A_{\rm ss}}{2D_{\rm ss}} - \frac{A_{\rm at}}{2D_{\rm at}}\right), \tag{56}$$

with

$$A_{\rm ss} = \rho_{\rm ss} + \rho_{\rm at}, \tag{57}$$
$$A_{\rm at} = 3A_{\rm ss} - 2. \tag{58}$$

Substituting Eqs. (50) and (56) into (39), we then obtain

$$\mathcal{A} = \frac{\psi L_{\eta,\rm sf}^{-1}}{l} - \frac{l(\rho_{\rm ss} - \rho_{\rm at})^2}{4}\left[\frac{s_{\rm v}A_{\rm ss}}{D_{\rm ss}} + \frac{\zeta}{T^2}\left(\frac{1}{2k_{\rm ss}} + \frac{1}{2k_{\rm at}}\right)\right], \tag{59}$$

with

$$\zeta = \frac{e_{\rm ht}^2}{l}\int_{-\infty}^{\infty}[1 - h^2(\rho)]\,dx = e_{\rm ht}^2 \tag{60}$$

and

$$\psi = l\int_{-\infty}^{\infty}[\eta'(x)]^2\,dx = 2/3, \tag{61}$$

also taking into account

$$\int_{-\infty}^{\infty}[[\rho(x)]^2 + g(\rho)[\rho(x)]^2 - 1]\,dx$$
$$= -\frac{3l}{4}A_{\rm ss}(\rho_{\rm ss} - \rho_{\rm at})^2, \tag{62}$$
$$\int_{-\infty}^{\infty}[[\rho(x)]^2[1 - g(\rho)]]\,dx = \frac{l}{4}A_{\rm at}(\rho_{\rm ss} - \rho_{\rm at})^2. \tag{63}$$

The functions defined in Eqs. (37) and (36) are again adopted to calculate integrals in Eqs. (61) and (60)–(63).

Therefore, in order to ensure $\mathcal{A} = 0$, we take

$$L_{\eta,\rm sf}^{-1} = \frac{l^2(\rho_{\rm ss} - \rho_{\rm at})^2}{4\psi}\left[\frac{s_{\rm v}A_{\rm ss}}{D_{\rm ss}} + \frac{\zeta}{T^2}\left(\frac{1}{2k_{\rm ss}} + \frac{1}{2k_{\rm at}}\right)\right]. \tag{64}$$

The mobility $L_{\eta,\rm gb}^{-1}$ of $\{\eta_i\}$ can be obtained from the physical grain boundary mobility $G_{\rm gb}^{\rm eff}$ and grain boundary energy $\gamma_{\rm gb}$ as

[8,55]

$$L_{\eta,\mathrm{gb}}^{-1} = \frac{\kappa_\eta}{G_{\mathrm{gb}}^{\mathrm{eff}}\gamma_{\mathrm{gb}}}. \tag{65}$$

Recalling Eqs. (16c) and (17), it is worth mentioning that this mobility is defined under the driving force represented by entropy, which should be distinguished from the original formulation in Ref. [55] as here κ_η adopts the dimension of the entropy per length. Accordingly, for L_η^{-1} as regards the full sintering description, we then take

$$L_\eta^{-1} = 16\rho^2(1-\rho)^2 L_{\eta,\mathrm{sf}}^{-1} + L_{\eta,\mathrm{gb}}^{-1}. \tag{66}$$

Recalling the anisotropic definitions of $\mathbf{L}_{\mathrm{ee}}$ and $\mathbf{L}_{\rho\rho}$ in Eqs. (42) and (51), calculation of $\hat{L}_\eta^{-1}$ in Eq. (17) can be further simplified as

$$\hat{L}_\eta^{-1} = L_\eta^{-1} - l^2|\nabla\rho|^2\left[M_1^2 L_{\rho\rho}^{\mathrm{v}} + M_2^2 L_{\mathrm{ee}}^{\perp}\right], \tag{67}$$

as $L_{\mathrm{ee}}^{\perp}$ and $L_{\rho\rho}^{\mathrm{v}}$ are, respectively, one of the eigenvalues of $\mathbf{L}_{\mathrm{ee}}$ and $\mathbf{L}_{\rho\rho}$, corresponding to the eigendirection of $\mathbf{n}_{\mathrm{sf}}$ ($\mathbf{n}_{\mathrm{sf}} \equiv \nabla\rho/|\nabla\rho|$).

It is worth noting that M_1 and M_2 are derived based on the constant postulate, i.e., M_1 and M_2 are spatiotemporal independent constants for a sintering system with known mass diffusivities and thermal conductivities of substance and atmosphere as well as given diffuse interface width, since the spatiotemporal dependency of all OP-related terms [Eqs. (48) and (49), (61), and (60)–(63)] vanish after integral. More importantly, the quantitative phase-field model degenerates to the conventional one when the system has no differences in mass diffusivity and thermal conductivity between solid and atmosphere. In that sense, when $D_{\mathrm{ss}} = D_{\mathrm{at}}$, $M_1 = 0$ and also when $k_{\mathrm{ss}} = k_{\mathrm{at}}$, $M_2 = 0$, demonstrating that the antitrapping terms in Eqs. (16a) and (16b) and the cross-coupling term in Eq. (16c) reduce to zero. In addition, we note that variational quantitative phase-field models such as the one presented in this work do not generally demonstrate high numerical accuracy [33,44,45]. Correct mapping of the variational model onto the associated sharp-interface equations only guarantees its quantitative validity and not its numerical efficiency needed for realistic utilization [44]. Therefore, a nonvariational form of the model might be best suited for practicability. The nonvariational form can be simply developed via modification of model parameters and functions while ensuring that the thin-interface asymptotic remains consistent.

V. RESULTS AND DISCUSSION

A. Model verification for an elliptical inclusion

To examine the capability of the model in ensuring $\delta\mu = \delta T = 0$ at the free surface, we perform diffusion-driven reshaping simulations of an elliptical inclusion with major axis A and minor axis B morphing into a circle. We set up a simulation domain with the lengths L_x and L_y in the x and y directions, respectively. The domain is further subjected to an initial temperature gradient $\nabla T = g_0$ along the x-axis. ρ is taken to vary smoothly from 1 in the inclusion ($\rho_{\mathrm{ss}} = 1$) to 0 outside ($\rho_{\mathrm{at}} = 0$) with $l = 1$. A full schematic of the simulation setup is given in Fig. 2(a). The normalized values of the employed model parameters are given in Table I.

TABLE I. Set of dimensionless quantities and parameters employed for the simulations in this work.

L_x	L_y	g_0	$\underline{C}$	$\underline{D}$	e_{ht}	$L_{\eta,\mathrm{gb}}$	s_{v}
60	50	0.01	1	0.062	1	1	1

First, we consider a case of asymmetric mass transport where $D_{\mathrm{at}}/D_{\mathrm{ss}} = 2$. We set $k_{\mathrm{at}}/k_{\mathrm{ss}} = 1$, hence only employing the mass antitrapping current term associated with mass diffusion while the thermal antitrapping current is tentatively dropped. The profile of chemical potential $\mu(x)$ across the moving free surface is presented for the cases $M_1 = 0$ and $M_1 \neq 0$ in Figs. 2(c) and 2(d), respectively. An extrapolation of $\mu(x)$ gives the chemical potential jump ($\delta\mu$) at the center of the free surface $\rho = 0.5$. Typically, $\delta\mu \neq 0$ implies an exchange of mass between the solid and atmosphere, which can be likened to the trans-interface diffusion phenomenon. However, no mass exchange is expected between the solid and atmosphere regions during sintering. Therefore, $\delta\mu = 0$ should be held in phase-field simulations in order to achieve realistic mass diffusion. It is obvious from Figs. 2(c) and 2(d) that the case with $M_1 = 0$ shows a significantly larger $\delta\mu$ compared to the one with $M_1 \neq 0$, in which the relatively small $\delta\mu$ is attributed to possible numerical errors. The results demonstrate that the mass antitrapping current parametrized by M_1 is necessary in order to eliminate the artificial diffusion flux across the interface during sintering for cases of asymmetric mass transport. Figures 2(c) and 2(d) also show the gap in space δx between the center of the free surface and the point where the extrapolations of μ meet. Note that $\delta x = 0$ when $\delta\mu = 0$, indicating the coherence between the numerically predicted interface by $\rho \approx 0.5$ and the theoretical sharp interface where $\delta\mu = 0$. Similar to $\delta\mu$, the numerical results demonstrate a significantly larger δx for the case with $M_1 = 0$ compared to the one with $M_1 \neq 0$, implying an apparent deviation in the position between the predicted interface and the theoretical sharp interface.

We also note the existence of another chemical potential drop $\Delta\mu$ across the free surface, characterizing the differences between the bulk values, as depicted in Figs. 2(c) and 2(d). This $\Delta\mu$, which is identical for both cases at a time point, was numerically examined to be the outcome of the deviated bulk values of ρ, i.e., ρ_{ss} and ρ_{at} that are slightly deviated from ideal (equilibrium) 1 and 0, respectively, as listed in Table S1 (see Supplemental Material [61]). Such a chemical potential drop generally does not appear in the conventional sharp-interface interpretation of the sintering [1,2]. Meanwhile, the deviated bulk values of the conserved mass OP have been depicted in previous works [56–60] with theoretical and numerical analyses given in Refs. [59] and [60], which are further discussed in the Appendix.

Furthermore, Fig. 2(b) shows a comparison of $\delta\mu$ versus diffuse interface width l between the cases with/without M_1 parametrized. It can be observed that both cases present the convergence $\delta\mu \to 0$ as $l \to 0$, replicating the sharp-interface condition when l tends to infinitesimal. However, as l increases, $\delta\mu$ presents a relatively rapid growth in the case with $M_1 = 0$ compared to the one with $M_1 \neq 0$, demonstrating that

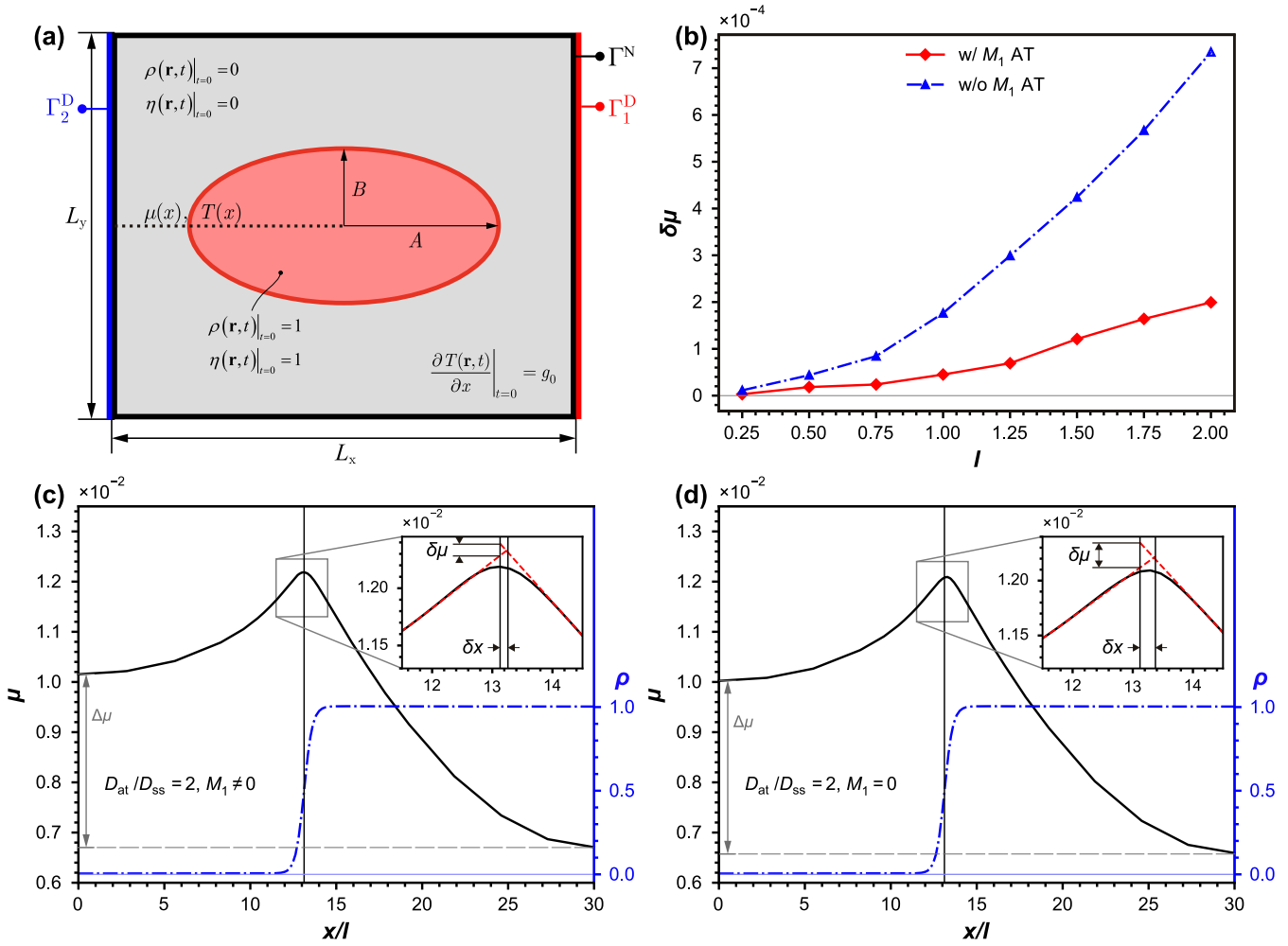

FIG. 2. (a) Schematic of the simulation setup in 2D simulation of an elliptical inclusion. (b) Comparison of chemical potential jump $\delta\mu$ across the free surface with respect to interface width; blue triangle symbols represent the model with $M_1 = 0$, while red diamond symbols represent the model with $M_1 \neq 0$. Plots of μ and ρ across the free surface as a function of x with $l = 1$, $D_{at}/D_{ss} = 2$ for (c) $M_1 \neq 0$ and (d) $M_1 = 0$. $\delta\mu$ is obtained using an extrapolation of μ at the center of the free surface $\rho = 0.5$. $\Delta\mu$ is the chemical potential difference between the bulk values.

the employment of mass antitrapping current parametrized by M_1 can significantly reduce the artificial interface effect (here the growing $\delta\mu$) along with increasing diffuse interface width. In this sense, mass antitrapping current allows reasonable quantitative simulations, especially at larger interface widths. Furthermore, we note that the convergence of both models might be well investigated considering a steady-state free surface velocity. We hope to report this in our upcoming work.

Additionally, we investigate a case of asymmetric heat transport with $k_{at}/k_{ss} = 0.05$. Similar to previous simulation, we examine the thermal antitrapping term associated with heat transport. The mass antitrapping term is tentatively dropped by setting $D_{at}/D_{ss} = 1$. Simulations are performed for the existing model (i.e., $M_2 = 0$) and the quantitative model with $M_2 \neq 0$. Further details of the results are given in the supplemental material (Fig. S2) [61]. $\delta T = 0$ realized at the sharp-interface is expected to be obtained during phase-field simulations in order to guarantee quantitative simulations. For the model with $M_2 = 0$, however, emerging $\delta T \neq 0$ demonstrates the importance of the thermal antitrapping current. Here, it is important to note that measured δT has a relatively low magnitude compared to the bulk temperature at the free surface. The importance of the thermal antitrapping term M_2 in eliminating the temperature jump for asymmetric heat transport has also been demonstrated in Ref. [41], where the nondiagonal phase-field model was also used.

B. Comparison between the quantitative and the existing models

In this section, we perform simulations for grain coalescence of two spherical grains with distinct sizes. Comparisons of microstructure and temperature distribution are made between the quantitative model where antitrapping terms are taken into account, and the existing model where these terms are not considered. The two models are referred to as the model with ATs and the model without ATs in the following discussions.

We set up a simulation domain with the lengths L_x and L_y in the x and y direction, respectively. Similar to the previous setup, the domain is subjected to $\nabla T = g_0$ along the x-axis. Simulations are performed for asymmetric mass and

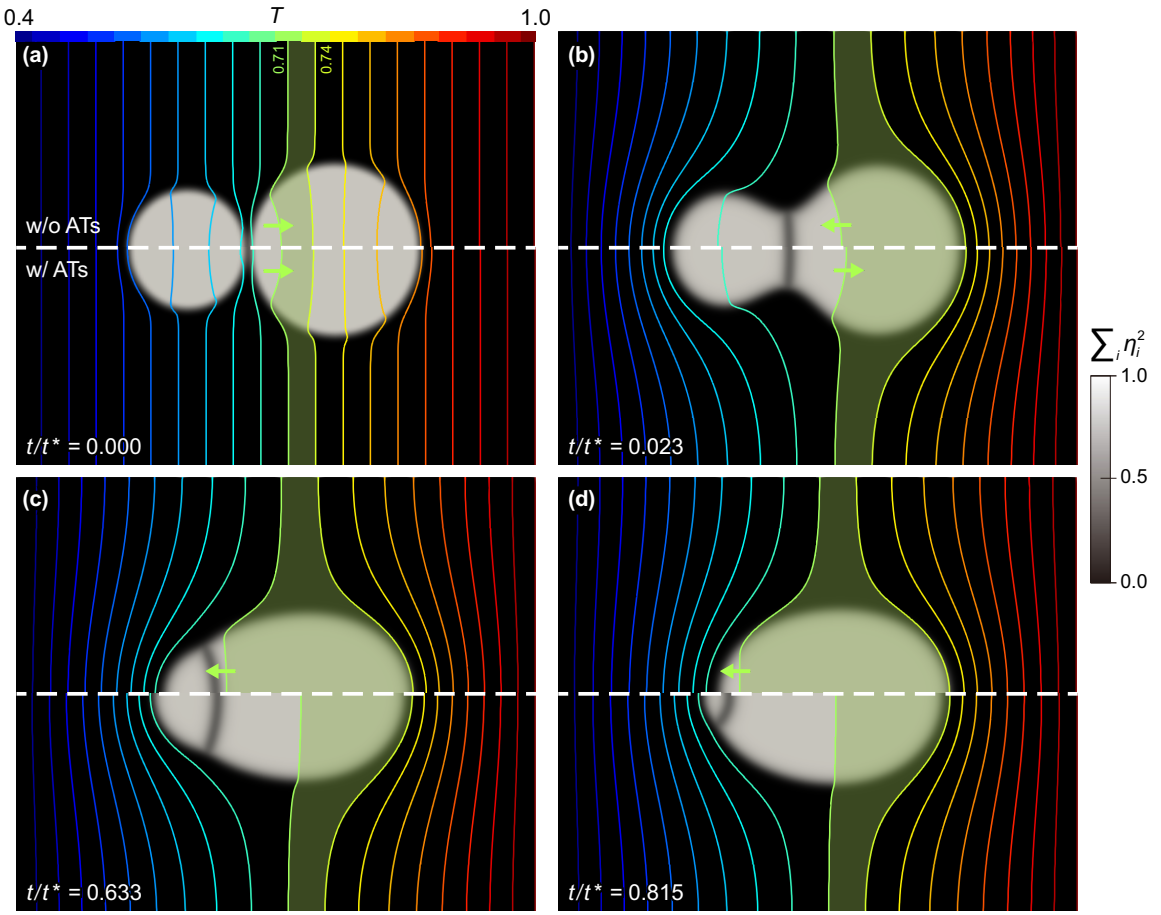

FIG. 3. Snapshots of grain coalescence of two spherical grains with distinct sizes. $D_{\mathrm{at}}/D_{\mathrm{ss}} = 2$, $l = 2$, and $k_{\mathrm{at}}/k_{\mathrm{ss}} = 0.05$ are set. Comparison is made between models with ATs and without ATs. Temperature isolines are also indicated. $t^* = 10^3$ unit.

heat transport where $D_{\mathrm{at}}/D_{\mathrm{ss}} = 2$, $k_{\mathrm{at}}/k_{\mathrm{ss}} = 0.05$ with $l = 2$. A full schematic of the simulation setup is supplemented in Fig. S4a (see Supplemental Material [61]).

Transient microstructures and temperature profiles for both models are compared and presented in Fig. 3. First, we observe that mass transport was faster for the model without ATs compared to the model with ATs. At $t/t^* = 0.633$ and 0.815 in Figs. 3(c) and 3(d), respectively, a more coalesced grain is obtained for the model without ATs compared to the model with ATs. The difference in progress of coalescence can be further explained by the visualization of mass diffusion fluxes at the free surface $\rho = 0.5$ as presented in Fig. 4. The free surface profile is colored by the local curvature calculated as $-\nabla \cdot \mathbf{n}_{\mathrm{sf}}$. Furthermore, mass diffusion fluxes are indicated at two distinct points, namely a concave point and a convex point. Typically, mass flux at any point on the free surface is expected to be correctly captured along the tangential direction to the free surface at that point. It can be clearly observed that $\mathbf{J}_\rho$, which is the mass diffusion flux without the mass antitrapping current, deviates in the direction from the tangential direction (dash-dotted lines) to the free surface at both the concave and the convex points. The mass antitrapping flux $\mathbf{J}_{\rho,\mathrm{AT}}$ introduced in the quantitative model can be seen flowing through the free surface in the normal direction from the solid grain region to the atmosphere. The combined mass flux $\mathbf{J}'_\rho = \mathbf{J}_\rho + \mathbf{J}_{\rho,\mathrm{AT}}$ shows a corrected mass flux flowing along the tangential direction to the free surface. Therefore, the deviation of $\mathbf{J}_\rho$ from its appropriate direction is due to the existence of a chemical potential jump at the free surface. $\mathbf{J}_{\rho,\mathrm{AT}}$ serves to eliminate this chemical potential jump, which consequently corrects this deviation. Accordingly, this

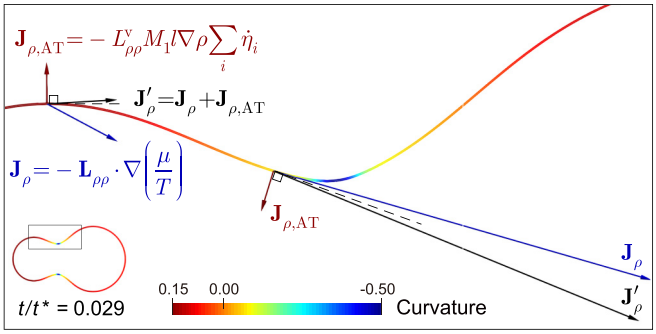

FIG. 4. Surface profile ($\rho = 0.5$) colored by the curvature and the mass diffusion fluxes, i.e., the fluxes before ($\mathbf{J}_\rho$) and after ($\mathbf{J}'_\rho$) correction with the antitrapping contribution ($\mathbf{J}_{\rho,\mathrm{AT}}$), at two distinct sites. The lengths of the visualized arrows have been scaled according to the magnitude of the fluxes uniformly.

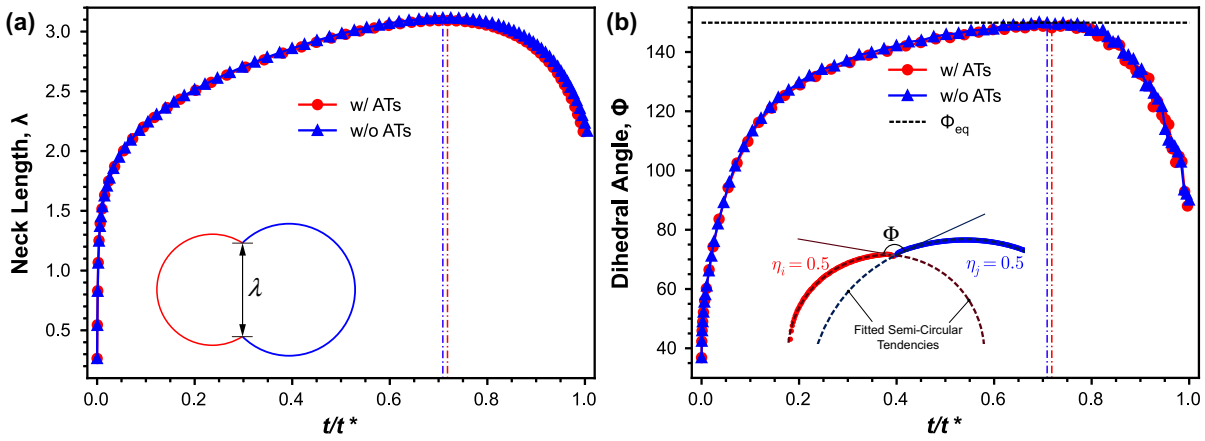

FIG. 5. Time evolution of (a) sintering neck λ and (b) dihedral angle Φ during the nonisothermal sintering process, as shown in Fig. 3. The time points reaching maximum values are indicated by colored vertical lines. The equilibrium dihedral angle Φ_{eq}, calculated from the surface and grain boundary energies, is also indicated by a black dotted line in (b). The total simulation time $t^* = 2084$ unit.

demonstrates the faster mass transport observed for the model without ATs. A chemical potential jump at the free surface tends to act as an extra driving force for grain coalescence leading to faster mass diffusion. The elimination of this jump via the antitrapping current leads to a slower mass transport for the model with ATs.

Furthermore, the results in Fig. 3 also show a comparison of the temperature profiles obtained for both models. The distribution of the temperature isolines shows faster heat transport for the model without ATs compared to the model with ATs. An example is given for isoline $T = 0.71$. Even though it initially tends to migrate towards the high-T side, at $t/t^* = 0.023$, this tendency stops for the model without ATs, where the isoline starts to move towards the low-T side, but it continues for the model with ATs. The result at $t/t^* = 0.815$ in Fig. 3(d) indicates a colder grain for the model with ATs compared to the model without ATs. Similar to the mass transport fluxes explanation for both models, the temperature jump at the free surface can be seen as an extra driving force for heat transport in the model without ATs. This jump is eliminated for the model with ATs via the thermal antitrapping term, thereby obtaining a slower heat transport. The presented thermal-microstructure evolution once more demonstrates the importance of the antitrapping currents for mass and heat diffusion.

We further examine the in-process sintering neck λ and dihedral angle Φ of the simulation as presented in Fig. 3. λ and Φ are calculated by

$$\lambda = \int_{\Omega} \frac{16 \sum_{i \neq j} \eta_i^2 \eta_j^2}{l} \, d\Omega,$$
$$\Phi = \arctan\left(\frac{\partial C_{\eta_i}}{\partial x}\right)_{\text{neck}} - \arctan\left(\frac{\partial C_{\eta_j}}{\partial x}\right)_{\text{neck}}, \tag{68}$$

where C_{η_i} and C_{η_j} are the fitted semicircular tendencies by coordinates of contour $\eta_i = 0.5$ and $\eta_j = 0.5$, respectively. $\frac{\partial C_{\eta_i}}{\partial x}$ and $\frac{\partial C_{\eta_j}}{\partial x}$ then provide the slopes of C_{η_i} and C_{η_j}. In this sense, Φ is calculated using the difference between these two angles of slope at the neck point, as shown in inset of Fig. 5(b), adapted from Ref. [62]. Meanwhile, the equilibrium dihedral angle Φ_{eq} can also be evaluated by the surface (γ_{sf}) and grain boundary (γ_{gb}) energies, i.e.,

$$\Phi_{eq} = 2 \arctan \frac{\gamma_{gb}}{2\gamma_{sf}}. \tag{69}$$

It is worth noting that Φ approaches Φ_{eq} when two particles with identical size are sintered isothermally, as λ reaches the maximum and stays constant, i.e., the system reaches equilibrium [8]. With varying interface width l, Φ deviates from the theoretically determined Φ_{eq} [Eq. (69)], as shown in Fig. S3 (see Supplemental Material [61]). This deviation is reduced in a similar fashion for both models with/without ATs as l decreases. This implies no modification to the thermodynamic equilibrium condition (characterized by Φ_{eq}) by applying the kinetic antitrapping terms. For two nonidentical grains, the time evolutions of λ and Φ are presented in Fig. 5. A comparison is made for the model with ATs and the model without ATs. It can be observed that for both models, Φ approaches Φ_{eq} at the points where λ attains maximum values. However, the progress of Φ towards Φ_{eq} is faster for the model without ATs compared to the model with ATs. This implies that while thermodynamic conditions are attained for both models, the antitrapping terms tend to modify the progress of neck growth and grain coalescence by removing the extra flux perpendicular to the free surface, as shown in Figs. 3 and 4.

C. Importance of anisotropic interpolations of the mobility tensor

Here, we demonstrate in particular the importance of the anisotropic interpolations of the kinetic mobilities. First, we investigate a steady-state heat-transfer case. The numerical validation test proposed by Nicoli *et al.* [52] is used and extended. We consider a square simulation domain defined as [0,1] and [0,1] in the x and y direction, respectively, and subjected to $\nabla T = -2$ along the x-axis. The domain consists of a stationary disk-shaped solid grain with radius R surrounded by an atmosphere region. A schematic of the simulation setup is supplemented in Fig. S5a (see Supplemental Material [61]). For $k_{at}/k_{ss} = 10$, four cases of thermal conductivity interpolations are examined. We consider the form of interpolation

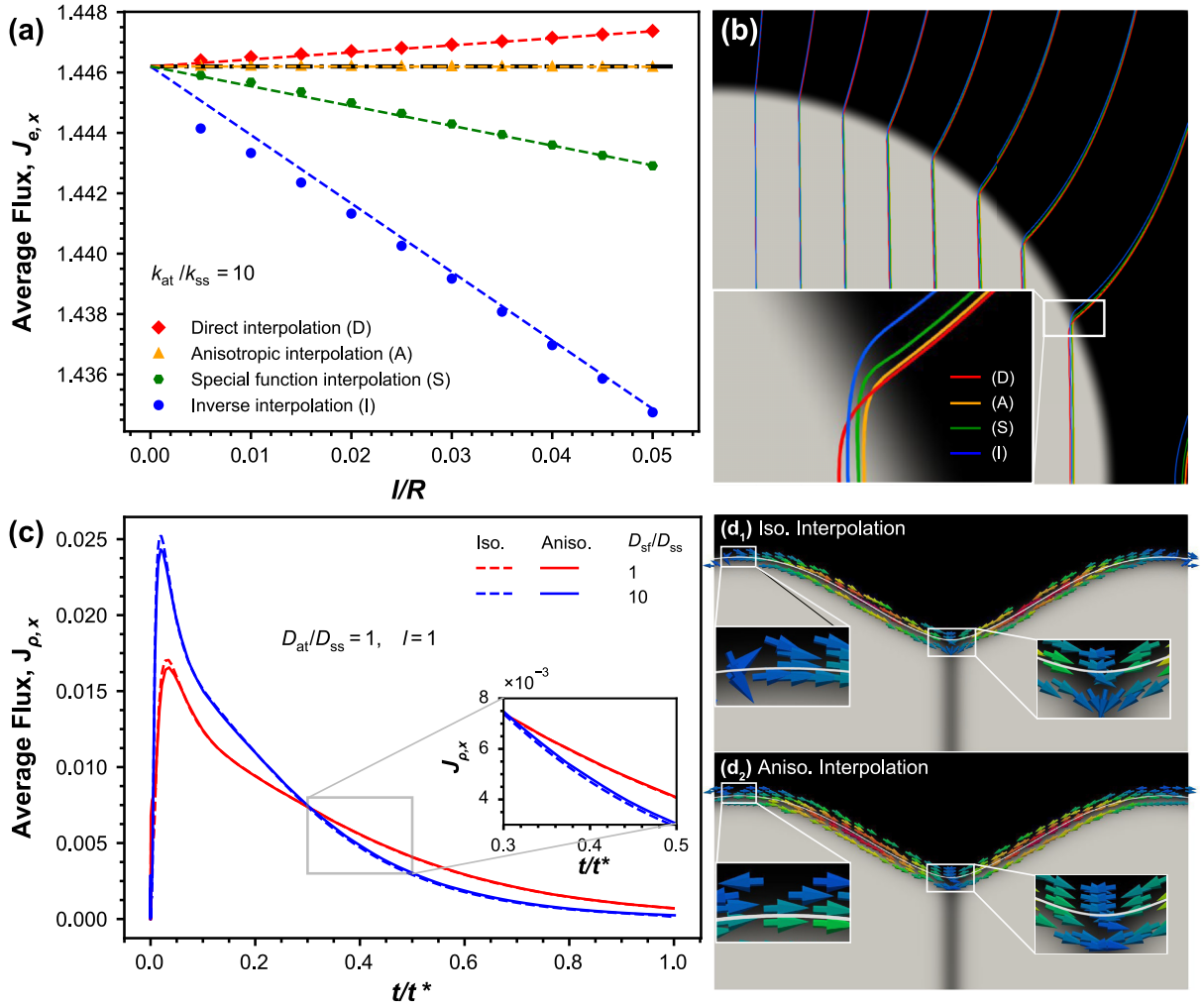

FIG. 6. (a) Comparison of $J_{e,x}$ vs l/R for different thermal conductivity interpolations: direct interpolation (red diamonds), inverse interpolation (blue circles), special function interpolation (green hexagons), and anisotropic interpolation (orange triangles) for $k_{at}/k_{ss} = 10$, where corresponding color lines are fitted simulation data lines, and black dash-dotted lines represent the plot of a case in which no artificial interface effects exist. (b) Temperature isolines across the free surface for different thermal conductivity interpolations at $l/R = 0.05$. (c) Time evolution of $J_{\rho,x}$ using different diffusivity interpolations: isotropic (dash-dotted lines) and anisotropic (solid lines) for varied values of D_{sf}/D_{ss}. Local zooms around the neck of the grains using (d_1) isotropic interpolation of diffusivity, and (d_2) anisotropic interpolation of diffusivity. $t^* = 14 \times 10^3$ unit.

utilized in the current phase-field models of nonisothermal sintering [8,28]. This interpolation form is similar to the formulation given in Eq. (44) and is thereafter referred to as the direct interpolation. Also, we consider another form of interpolation given in Ref. [63] to ensure heat flux conservation across the interface. This form of interpolation, thereafter referred to as the inverse interpolation, has its formulation as in Eq. (43). Moreover, a form of interpolation proposed by Almgren [30] was used in Refs. [41] and [43] for their nondiagonal phase-field models. The interpolation, thereafter called the special function (SF) interpolation, is also examined and can be expressed as

$$\frac{1}{k(\rho)} = \left(\frac{1}{2k_{ss}} + \frac{1}{2k_{at}}\right) + p_{sf}(\rho)\left(\frac{1}{2k_{ss}} - \frac{1}{2k_{at}}\right), \tag{70}$$

with

$$p_{sf}(\rho) = (2\rho - 1)[1 + 4a\rho(1-\rho)], \tag{71}$$

where $a \approx 0.90$ for $k_{at}/k_{ss} = 10$. Here, it is important to note that the formulation in Eq. (70) is adopted from Ref. [43] because ϕ in Ref. [43] varies from 0 to 1 similar to ρ. Lastly, we consider the anisotropic form of thermal conductivity proposed in this work as expressed in Eq. (42). Artificial interface effects are quantified by obtaining the average heat flux, $J_{e,x}$, in the domain at $x = 1$. The plot of $J_{e,x}$ against normalized interface widths l/R is presented in Fig. 6(a) for different interpolation forms. The black line in Fig. 6(a) indicates a reference case where no artificial interface effect exists, i.e., $J_{e,x}\,|_{l=0} = J_{e,x}\,|_{l>0}$. Figure 6(b) shows the temperature isolines across the free surface for the different interpolation forms. As shown in Fig. 6(a), the direct and inverse interpolations show significant deviations from the reference case, implying the deficit of these interpolation forms in eliminating interface effects. The SF interpolation also shows considerable deviation from the reference case. This deviation, which might be attributed to the nonmonotonic form of $p_{sf}(\rho)$ [44],

reinforces the limitation of the SF interpolation. On the other hand, the results obtained by using the anisotropic interpolation show very convincing agreement. The outstanding performance of the anisotropic form of interpolation necessitates its consideration for subsequent nondiagonal phase-field modeling. Note that for common sintering scenarios (the result is supplemented in Fig. S5b (see Supplemental Material [61]) for $k_{at}/k_{ss} = 0.2$), the SF interpolation might be utilized for quantitative simulations. The anisotropic form of interpolation, however, finds great importance in other processes where k_{at}/k_{ss} is higher, such as the case studies in Ref. [64].

Also, we consider mass transport during grain coalescence of two identical spheres using two mass diffusivity interpolations. A full schematic of the simulation setup is supplemented in Fig. S4b (see Supplemental Material [61]). We make comparisons between the anisotropic interpolation presented in this work, Eq. (51), and an isotropic interpolation expressed as [15]

$$D = p_{ss}(\rho)D_{ss} + p_{at}(\rho)D_{at} + p_{sf}(\rho)D_{sf} + p_{gb}(\eta_i)D_{gb}, \quad (72)$$

where $p_{ss}(\rho)$ and $p_{at}(\rho)$ are interpolation functions valued as 1 only in the solid phase and atmosphere region, respectively. Average mass flux $J_{\rho,x}$ is obtained across a grain with the plots of $J_{\rho,x}$ against normalized time t shown in Fig. 6(c).

The thin-interface limit analysis showed that eliminating the chemical potential jump across the free surface does not require a specific mass diffusivity interpolation. Correspondingly, it has been derived in Refs. [65,66] that the Cahn-Hilliard equation recovers the sharp-interface limit equation of motion for surface diffusion regardless of the mass diffusivity form. Therefore, the $J_{\rho,x}$ versus t curve is expected to be the same for both interpolations of mass diffusivity, since theoretically no artificial interface effect is related to the diffusivity interpolation. However, as shown in Fig. 6(c), there exist surprisingly $J_{\rho,x}$ numerical deviations. This can be explained by close comparison of flux details at the free surface region. Figures 6(d_1) and 6(d_2) demonstrate the calculated flux by using the isotropic and anisotropic diffusivity form, respectively. We observe that the anisotropic form of diffusivity delivers a more reasonable description of the directions of the fluxes. Around the free surface in Fig. 6(d_1) where we used isotropic diffusivity, there exist nontangential fluxes at the free surface where only tangential fluxes are expected to contribute to surface diffusion. On the other hand, in Fig. 6(d_2) where the anisotropic diffusivity form is used, only fluxes that are tangential to the free-surface region exist to describe surface diffusion. Accordingly, it is imperative that, while asymptotic analysis confers no restriction on the diffusivity form as regards effecting quantitative simulations in mass diffusion, the anisotropic diffusivity form makes it possible that the directions of fluxes are effectively described analogous to the sharp-interface description.

VI. CONCLUSIONS

In this work, we have developed a variational quantitative phase-field model for nonisothermal sintering processes following the nondiagonal phase-field approach introduced in Refs. [37,39]. The model was formulated to eliminate artificial interface effects due to the diffuse-interface description of the free surfaces. Moreover, model formulations are derived in a variational manner guaranteeing thermodynamic consistency. The proposed model differs from conventional nonisothermal sintering models due to that fact that cross-coupling terms between conserved kinetics (mass and heat transfer) and the nonconserved kinetics (grain growth) are taken into the account. These terms parametrized by functions M_1 and M_2 can be likened to antitrapping currents in quantitative phase-field modeling. The above-mentioned terms are particularly essential for correct projection of the model to its sharp-interface descriptions. Also, we derive formulations of M_1 and M_2 in terms of the model parameters using an asymptotic analysis procedure presented in Ref. [38]. In addition, we showed that anisotropic interpolations of kinetic mobilities are also important to ascertain the elimination of artificial interface effects at the free surface.

Numerical tests were done to highlight the importance of these cross-coupling terms. The results presented showed the emergence of a chemical potential jump ($\delta\mu$) and a temperature jump (δT) at the free surface when $M_1 = 0$ and $M_2 = 0$. $\delta\mu \neq 0$ and $\delta T \neq 0$ negate the sharp-interface sintering description. However, employing $M_1 \neq 0$ and $M_2 \neq 0$ as described in the quantitative model eliminates these jumps. The convergence behavior of $\delta\mu$ with respect to interface width (l) was presented for the model with $M_1 = 0$ and the model with $M_1 \neq 0$. For both models, $\delta\mu \to 0$ as $l \to 0$, demonstrating their efficacy at relatively smaller l. The major usefulness of the quantitative model is seen as $l \gg 0$, where $\delta\mu$ is significantly large for the model with $M_1 = 0$ compared to the model where $M_1 \neq 0$. Additionally, the difference in transient microstructure and temperature profiles was examined for the model with antitrapping currents and the model without antitrapping currents. It was seen that the antitrapping currents help to eliminate extra driving forces brought about by $\delta\mu \neq 0$ and $\delta T \neq 0$ at the free surface. Moreover, it was demonstrated that the antitrapping currents only modify the sintering kinetics and have no impact on the thermodynamic conditions.

Furthermore, we demonstrated numerically how the anisotropic interpolation of kinetic mobilities delivers an effective description of diffusion fluxes comparable to the sharp-interface description. Therefore, the proposed model can serve as a great tool in studying quantitative simulations of nonisothermal sintering and other related solid-state processes. A major outlook of this work is to further investigate the convergence of interface velocity with respect to interface width obtained using the proposed model.

The authors declare that the data supporting the findings of this study are available within the paper. Source codes of MOOSE-based application NIsoS and related utilities are provided in the online repository in Ref. [67].

ACKNOWLEDGMENTS

The authors acknowledge the financial support of German Science Foundation (DFG) in the Priority Program 2256 (SPP 2256, Project No. 441153493) and Collaborative Research center Transregio 270 (CRC-TRR 270, Project No. 405553726, subprojects A06). The authors also greatly appreciate their access to the Lichtenberg II High-Performance

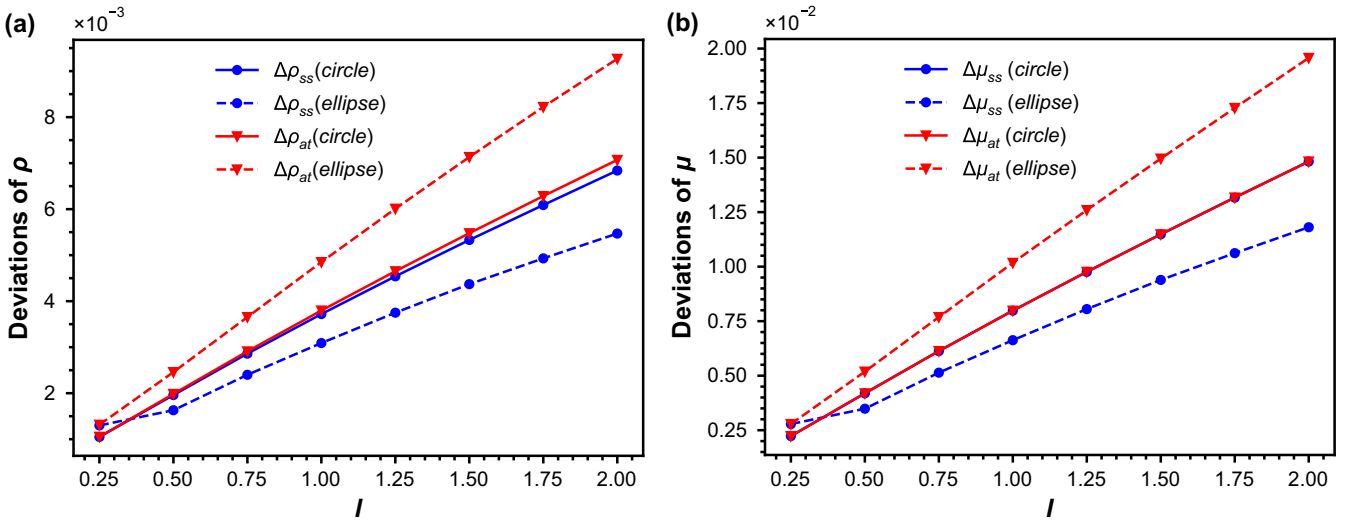

FIG. 7. The deviated bulk values of (a) ρ and (b) μ with respect to the diffuse interface width l. The deviated bulk values are read from the numerical results presented in Fig. 2(a).

Computer (HPC) and the technical support from the HHLR, Technische Universität Darmstadt. The computation time on the HPC is granted by the NHR4CES Resource Allocation Board under the Project: special00007.

APPENDIX: DEVIATION OF CONSERVED ORDER PARAMETER

The analyses of Cahn-Hilliard dynamics in Refs. [59] and [60] have shown that usage of a finite interface width combined with a comparable curvature radius induces deviation of the conserved order parameter (ρ in this work) in the bulk regions. It has been demonstrated that the equilibrium bulk values of ρ are contingent on the interface having negligible volume compared to the bulk region, so that only the local free energy finds minimization. Although this condition is viable for planar interfaces, it is not maintained for curved interfaces with concentrated energy. In this sense, the total free energy can be reduced by shrinking the area enclosed by the interface, which subsequently shifts the bulk values of ρ from the equilibrium ones due to the finite volume precept [59]. Here, we define the deviated quantities of ρ from its equilibrium values (in this work, $\rho_{\mathrm{ss}}^{\mathrm{eq}} = 1$ and $\rho_{\mathrm{at}}^{\mathrm{eq}} = 0$) as $\Delta\rho_{\mathrm{ss}} = \rho_{\mathrm{ss}} - 1$ and $\Delta\rho_{\mathrm{at}} = \rho_{\mathrm{at}}$. Both ρ_{ss} and ρ_{at} are read from numerical results in Fig. 2(a) with $M_1 = 0$ when the particle is in elliptical and circular shapes. The tendencies of $\Delta\rho_{\mathrm{ss}}$ and $\Delta\rho_{\mathrm{at}}$ versus l are shown in Fig. 7(a). Similar to results obtained in Ref. [59], $\Delta\rho_{\mathrm{ss}}$ and $\Delta\rho_{\mathrm{at}}$ increase with increasing l. When in the elliptical shape (implying a nonequilibrium condition), $\Delta\rho_{\mathrm{at}} > \Delta\rho_{\mathrm{ss}}$ holds for almost every selected l, while $\Delta\rho_{\mathrm{ss}} \approx \Delta\rho_{\mathrm{at}}$ when in the circular shape (implying an equilibrium condition). These differences can be attributed to the curvature dependency of the analytical profile of ρ [60]. It should be noted that $\Delta\rho_{\mathrm{ss}}$ and $\Delta\rho_{\mathrm{at}}$ exist even for symmetric

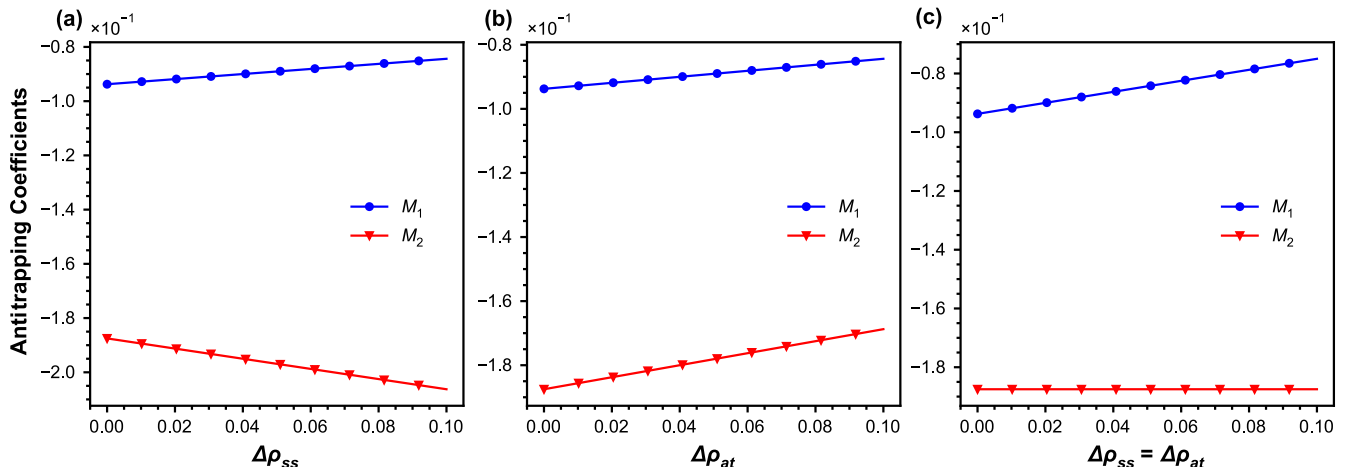

FIG. 8. The antitrapping coefficients M_1 and M_2 with respect to (a) varying $\Delta\rho_{\mathrm{ss}}$ when $\Delta\rho_{\mathrm{at}} = 0$, (b) varying $\Delta\rho_{\mathrm{at}}$ when $\Delta\rho_{\mathrm{ss}} = 0$, and (c) varying simultaneously $\Delta\rho_{\mathrm{ss}}$ and $\Delta\rho_{\mathrm{at}}$ while holding $\Delta\rho_{\mathrm{ss}} = \Delta\rho_{\mathrm{at}}$.

mobilities with sufficiently large l, which is distinctive from the known interface effects (such as trap effects) that are incited by asymmetric kinetic mobilities. Moreover, the comparison of analytical values of $\Delta\rho_{ss}$ and $\Delta\rho_{at}$ and numerical values should be examined in further studies.

As one of the significant outcomes, deviated bulk values of ρ incite deviated chemical potential μ from its equilibrium ones in the bulk regions, which may result in the unexpected chemical potential drop as an extra driving force across the free surface. To examine this point, we define the deviated quantities of μ in a similar fashion to $\Delta\rho_{ss}$ and $\Delta\rho_{at}$, i.e., $\Delta\mu_{ss} = \mu_{ss}(\rho_{ss}) - \mu^{eq} = \mu_{ss}(\rho_{ss})$ and $\Delta\mu_{at} = \mu_{at}(\rho_{at}) - \mu_{at}^{eq} = \mu_{at}(\rho_{at})$, noting that $\mu_{ss}^{eq}(\rho_{ss}^{eq} = 1) = \mu_{at}^{eq}(\rho_{at}^{eq} = 0) = 0$. In Fig. 7(b), we present a similar tendency of $\Delta\mu_{ss}$ and $\Delta\mu_{at}$ versus l when the particle is in the elliptical shape, where both $\Delta\mu_{ss}$ and $\Delta\mu_{at}$ grow along with increasing l, and $\Delta\mu_{ss} > \Delta\mu_{at}$ is depicted for every selected l, implying the existing chemical potential drop $\Delta\mu = \Delta\mu_{at} - \Delta\mu_{ss} > 0$ across the free surface at the semimajor axis, as shown in Fig. 2(a). Notably, when the particle is in the circular shape, $\Delta\mu_{ss} = \Delta\mu_{at}$ is formed without the dependency of l, indicating no chemical potential drop across the free surface, i.e., $\Delta\mu = \Delta\mu_{at} - \Delta\mu_{ss} = 0$. This also demonstrates that the existing deviation in μ incited by $\Delta\rho_{ss}$ and $\Delta\rho_{at}$ does not affect the supposed equilibrium condition, as the particle stops morphing in the circular shape.

Additionally, since the antitrapping coefficients M_1 and M_2 are dependent on the bulk values ρ_{ss} and ρ_{at}, we examine the variations of M_1 and M_2 with $\Delta\rho_{ss}$ and $\Delta\rho_{at}$ up to 0.1, as seen in Fig. 8. In Fig. 8(a), we take $\Delta\rho_{at} = 0$ and examine the variations of M_1 and M_2 with $\Delta\rho_{ss}$. Similarly, we take $\Delta\rho_{ss} = 0$ and examine the variations of M_1 and M_2 with $\Delta\rho_{at}$ in Fig. 8(b). Then, we present the variations of M_1 and M_2 with $\Delta\rho_{ss} = \Delta\rho_{at}$ in Fig. 8(c). This demonstrates that M_1 presents a linear tendency versus increasing deviations of all cases. M_2, however, decreases along with growing $\Delta\rho_{ss}$ but increases with growing $\Delta\rho_{at}$. For $\Delta\rho_{ss} = \Delta\rho_{at}$, M_2 stays constant. This can be explained via Eq. (50), where M_2 is proportional to $(\rho_{ss} - \rho_{at})$, which is reduced to 1 when $\Delta\rho_{ss} = \Delta\rho_{at}$ as $(\rho_{ss} - \rho_{at}) = [(\Delta\rho_{ss} + 1) - \Delta\rho_{at}] = 1$.

[1] R. German, *Sintering: From Empirical Observations to Scientific Principles* (Butterworth-Heinemann, Oxford, 2014)

[2] S.-J. Kang, *Sintering: Densification, Grain Growth and Microstructure* (Elsevier, Amsterdam, 2004)

[3] W. Niu and J. Pan, 4–Computer modelling of sintering: Theory and examples, in *Sintering of Advanced Materials*, Woodhead Publishing Series in Metals and Surface Engineering, edited by Z. Z. Fang (Woodhead, Sawston, 2010), pp. 86–109.

[4] M. Yu, S. Grasso, R. Mckinnon, T. Saunders, and M. J. Reece, Review of flash sintering: materials, mechanisms and modelling, Adv. Appl. Ceram. **116**, 24 (2017).

[5] Z. A. Munir, U. Anselmi-Tamburini, and M. Ohyanagi, The effect of electric field and pressure on the synthesis and consolidation of materials: A review of the spark plasma sintering method., J. Mater. Sci. **41**, 763 (2006).

[6] D. D. Gu, W. Meiners, K. Wissenbach, and R. Poprawe, Laser additive manufacturing of metallic components: materials, processes and mechanisms, Int. Mater. Rev. **57**, 133 (2012).

[7] F. Pinto, R. Silva, and F. La Porta, Overview of conventional and unconventional sintering methods, in *Green Sustainable Process for Chemical and Environmental Engineering and Science* (Elsevier, Amsterdam, 2021), pp. 15–35.

[8] Y. Yang, T. D. Oyedeji, P. Kühn, and B.-X. Xu, Investigation on temperature-gradient-driven effects in unconventional sintering via non-isothermal phase-field simulation, Scr. Mater. **186**, 152 (2020).

[9] J. Frenkel, Viscous flow of crystalline bodies under the action of surface tension, J. Phys. (USSR) **9**, 385 (1945).

[10] G. Kuczynski, Self-diffusion in sintering of metallic particles, JOM **1**, 169 (1949).

[11] C. Smith, Grains, phases, and interfaces: an interpretation of microstructure, Trans. TMS-AIME **175**, 15 (1948).

[12] R. L. Coble, Sintering crystalline solids. I. Intermediate and final state diffusion models, J. Appl. Phys. **32**, 787 (1961).

[13] J. Mackenzie and R. Shuttleworth, A phenomenological theory of sintering, Proc. Phys. Soc. Sec. B **62**, 833 (1949).

[14] A. Kazaryan, Y. Wang, and B. R. Patton, Generalized phase field approach for computer simulation of sintering: incorporation of rigid-body motion, Scr. Mater. **41**, 487 (1999).

[15] Y. U. Wang, Computer modeling and simulation of solid-state sintering: A phase field approach, Acta Mater. **54**, 953 (2006).

[16] V. Kumar, Z. Z. Fang, and P. C. Fife, Phase field simulations of grain growth during sintering of two unequal-sized particles, Mater. Sci. Eng. A **528**, 254 (2010).

[17] K. Ahmed, C. A. Yablinsky, A. Schulte, T. Allen, and A. El-Azab, Phase field modeling of the effect of porosity on grain growth kinetics in polycrystalline ceramics, Modell. Simul. Mater. Sci. Eng. **21**, 065005 (2013).

[18] J. Deng, A phase field model of sintering with direction-dependent diffusion, Mater. Trans. **53**, 385 (2012).

[19] Y. Yang, M. Yi, B.-X. Xu, and L.-Q. Chen, Phase-field modeling of non-isothermal grain coalescence in the unconventional sintering techniques, arXiv:1806.02799 [cond-mat.mtrl-sci].

[20] S. Biswas, D. Schwen, and V. Tomar, Implementation of a phase field model for simulating evolution of two powder particles representing microstructural changes during sintering, J. Mater. Sci. **53**, 5799 (2018).

[21] Phase field modeling of sintering: Role of grain orientation and anisotropic properties, Comput. Mater. Sci. **148**, 307 (2018).

[22] K. Chockalingam, V. G. Kouznetsova, O. van der Sluis, and M. G. Geers, 2D Phase field modeling of sintering of silver nanoparticles, Comput. Methods Appl. Mech. Eng. **312**, 492 (2016).

[23] K. Ahmed, J. Pakarinen, T. Allen, and A. El-Azab, Phase field simulation of grain growth in porous uranium dioxide, J. Nucl. Mater. **446**, 90 (2014).

[24] R. Mukherjee, T. Chakrabarti, E. A. Anumol, T. A. Abinandanan, and N. Ravishankar, Thermal stability of spherical nanoporous aggregates and formation of hollow structures by sintering-a phase-field study, ACS Nano **5**, 2700 (2011).

[25] Three-dimensional phase field sintering simulations accounting for the rigid-body motion of individual grains, Comput. Mater. Sci. **186**, 109963 (2021).

[26] J. Hötzer, M. Seiz, M. Kellner, W. Rheinheimer, and B. Nestler, Phase-field simulation of solid state sintering, Acta Mater. **164**, 184 (2019).
[27] I. Greenquist, M. R. Tonks, L. K. Aagesen, and Y. Zhang, Development of a microstructural grand potential-based sintering model, Comput. Mater. Sci. **172**, 109288 (2020).
[28] Y. Yang, O. Ragnvaldsen, Y. Bai, M. Yi, and B.-X. Xu, 3D non-isothermal phase-field simulation of microstructure evolution during selective laser sintering, npj Comput. Mater. **5**, 81 (2019).
[29] X. Zhou, Y. Yang, S. Bharech, B. Lin, J. Schröder, and B.-X. Xu, 3d-multilayer simulation of microstructure and mechanical properties of porous materials by selective sintering, GAMM-Mitteilungen **44**, e202100017 (2021).
[30] R. Almgren, Second-order phase field asymptotics for unequal conductivities, SIAM J. Appl. Math. **59**, 2086 (1999).
[31] G. McFadden, A. Wheeler, and D. Anderson, Thin interface asymptotics for an energy/entropy approach to phase-field models with unequal conductivities, Physica D **144**, 154 (2000).
[32] A. Karma and W.-J. Rappel, Phase-field method for computationally efficient modeling of solidification with arbitrary interface kinetics, Phys. Rev. E **53**, R3017(R) (1996).
[33] A. Karma and W.-J. Rappel, Quantitative phase-field modeling of dendritic growth in two and three dimensions, Phys. Rev. E **57**, 4323 (1998).
[34] A. Karma, Phase-Field Formulation for Quantitative Modeling of Alloy Solidification, Phys. Rev. Lett. **87**, 115701 (2001).
[35] M. Ohno and K. Matsuura, Quantitative phase-field modeling for dilute alloy solidification involving diffusion in the solid, Phys. Rev. E **79**, 031603 (2009).
[36] M. Ohno, Quantitative phase-field modeling of nonisothermal solidification in dilute multicomponent alloys with arbitrary diffusivities, Phys. Rev. E **86**, 051603 (2012).
[37] E. A. Brener and G. Boussinot, Kinetic cross coupling between nonconserved and conserved fields in phase field models, Phys. Rev. E **86**, 060601(R) (2012).
[38] G. Boussinot and E. A. Brener, Interface kinetics in phase-field models: Isothermal transformations in binary alloys and step dynamics in molecular-beam epitaxy, Phys. Rev. E **88**, 022406 (2013).
[39] A. Fang and Y. Mi, Recovering thermodynamic consistency of the antitrapping model: A variational phase-field formulation for alloy solidification, Phys. Rev. E **87**, 012402 (2013).
[40] G. Boussinot and E. A. Brener, Achieving realistic interface kinetics in phase-field models with a diffusional contrast, Phys. Rev. E **89**, 060402(R) (2014).
[41] G. Boussinot, E. A. Brener, C. Hüter, and R. Spatschek, Elimination of surface diffusion in the non-diagonal phase field model, Contin. Mech. Thermodyn. **29**, 969 (2017).
[42] K. Wang, G. Boussinot, C. Hüter, E. A. Brener, and R. Spatschek, Modeling of dendritic growth using a quantitative nondiagonal phase field model, Phys. Rev. Mater. **4**, 033802 (2020).
[43] K. Wang, G. Boussinot, E. A. Brener, and R. Spatschek, Quantitative nondiagonal phase field modeling of eutectic and eutectoid transformations, Phys. Rev. B **103**, 184111 (2021).
[44] M. Ohno, T. Takaki, and Y. Shibuta, Variational formulation and numerical accuracy of a quantitative phase-field model for binary alloy solidification with two-sided diffusion, Phys. Rev. E **93**, 012802 (2016).
[45] M. Ohno, T. Takaki, and Y. Shibuta, Variational formulation of a quantitative phase-field model for nonisothermal solidification in a multicomponent alloy, Phys. Rev. E **96**, 033311 (2017).
[46] E. A. Olevsky, Theory of sintering: from discrete to continuum, Mater. Sci. Eng.: R **23**, 41 (1998).
[47] S. G. Kim, W. T. Kim, and T. Suzuki, Phase-field model for binary alloys, Phys. Rev. E **60**, 7186 (1999).
[48] B. Echebarria, R. Folch, A. Karma, and M. Plapp, Quantitative phase-field model of alloy solidification, Phys. Rev. E **70**, 061604 (2004).
[49] A. L. Maximenko and E. A. Olevsky, Effective diffusion coefficients in solid-state sintering, Acta Mater. **52**, 2953 (2004).
[50] S. Balibar, H. Alles, and A. Y. Parshin, The surface of helium crystals, Rev. Mod. Phys. **77**, 317 (2005).
[51] E. A. Brener and D. E. Temkin, Onsager approach to the one-dimensional solidification problem and its relation to the phase-field description, Phys. Rev. E **85**, 031601 (2012).
[52] M. Nicoli, M. Plapp, and H. Henry, Tensorial mobilities for accurate solution of transport problems in models with diffuse interfaces, Phys. Rev. E **84**, 046707 (2011).
[53] M. R. Tonks, Y. Zhang, A. Butterfield, and X.-M. Bai, Development of a grain boundary pinning model that considers particle size distribution using the phase field method, Modell. Simul. Mater. Sci. Eng. **23**, 045009 (2015).
[54] L. Zhang, M. R. Tonks, P. C. Millett, Y. Zhang, K. Chockalingam, and B. Biner, Phase-field modeling of temperature gradient driven pore migration coupling with thermal conduction, Comput. Mater. Sci. **56**, 161 (2012).
[55] N. Moelans, B. Blanpain, and P. Wollants, Quantitative analysis of grain boundary properties in a generalized phase field model for grain growth in anisotropic systems, Phys. Rev. B **78**, 024113 (2008).
[56] D. Jacqmin, Calculation of two-phase navier–stokes flows using phase-field modeling, J. Comput. Phys. **155**, 96 (1999).
[57] P. Yue, J. J. Feng, C. Liu, and J. Shen, A diffuse-interface method for simulating two-phase flows of complex fluids, J. Fluid Mech. **515**, 293 (1999).
[58] J. J. Feng, C. Liu, J. Shen, and P. Yue, An energetic variational formulation with phase field methods for interfacial dynamics of complex fluids: advantages and challenges, in *Modeling of Soft Matter* (Springer, Berlin, 2005), pp. 1–26.
[59] P. Yue, C. Zhou, and J. J. Feng, Spontaneous shrinkage of drops and mass conservation in phase-field simulations, J. Comput. Phys. **223**, 1 (2007).
[60] A. Dadvand, M. Bagheri, N. Samkhaniani, H. Marschall, and M. Wörner, Advected phase-field method for bounded solution of the cahn-hilliard navier-stokes equations, Phys. Fluids **33**, 053311 (2021).
[61] See Supplemental Material at http://link.aps.org/supplemental/10.1103/PhysRevE.108.025301 for additional details, such as simulation set ups, results of the thermal antitrapping term simulations, values of the deviated bulk values of ρ, as well as more details on the mobility interpolation forms.
[62] N. Moelans, F. Wendler, and B. Nestler, Comparative study of two phase-field models for grain growth, Comput. Mater. Sci. **46**, 479 (2009).
[63] A. Aalilija, C.-A. Gandin, and E. Hachem, A simple and efficient numerical model for thermal contact resistance based on

diffuse interface immersed boundary method, Int. J. Therm. Sci. **166**, 106817 (2021).

[64] Y. Yang, M. Fathidoost, T. D. Oyedeji, P. Bondi, X. Zhou, H. Egger, and B.-X. Xu, A diffuse-interface model of anisotropic interface thermal conductivity and its application in thermal homogenization of composites, Scr. Mater. **212**, 114537 (2022).

[65] C. Gugenberger, R. Spatschek, and K. Kassner, Comparison of phase-field models for surface diffusion, Phys. Rev. E **78**, 016703 (2008).

[66] K. Ahmed, T. Allen, and A. El-Azab, Phase field modeling for grain growth in porous solids, J. Mater. Sci. **51**, 1261 (2016).

[67] bitbucket.org/mfm_tuda/nisos.git.